

# A Fast Algorithm for Automatic Segmentation and Extraction of A Single Object By Active Surfaces

Jianping Zhang\*, Ke Chen<sup>†</sup> and Derek A. Gould<sup>‡</sup>

## Abstract

Segmentation is an important problem in various applications. There exist many effective models designed to locate all features and their boundaries in an image. However such global models are not suitable for automatically detecting a single object among many objects of an image, because nearby objects are often selected as well. Several recent works can provide selective segmentation capability but unfortunately when generalized to three dimensions, they are not yet effective or efficient. This paper presents a selective segmentation model which is inherently suited for efficient implementation. With the added solver by a fast nonlinear multigrid method for the inside domain of a zero level set function, the over methodology leads to an effective and efficient algorithm for 3D selective segmentation. Numerical experiments show that our model can produce efficient results in terms of segmentation quality and reliability for a large class of 3D images.

**AMS** 62H35, 65N22, 65N55, 74G65, 74G75.

**Keywords.** Active surfaces, local energy function, partial differential equations, 3D segmentation, level sets, geometric constraints, evolution equation.

## 1 Introduction

Segmentation is an important task in image analysis and computer vision, aiming to partition a given image into a finite number of semantically important regions such as homogenous regions or structures. This paper is particularly concerned with modeling and fast algorithms for local segmentation or extraction of a single region in an image.

Although local segmentation is less studied than and is quite different from the usual global segmentation, they are intrinsically linked. Among other techniques, two problems can be solved by variational methods using global optimization ideas as increasingly used to detect objects in the past two decades (due to their robustness and reliability). As demonstrated shortly, global models must be modified fundamentally in order to solve local segmentation problems.

---

\*Centre for Mathematical Imaging Techniques and Department of Mathematical Sciences, University of Liverpool, United Kingdom and School of Mathematics and Computational Science, Xiangtan University, Xiangtan, Hunan 411105, P. R. China

<sup>†</sup>Centre for Mathematical Imaging Techniques and Department of Mathematical Sciences, University of Liverpool, United Kingdom. Corresponding Email: k.chen@liverpool.ac.uk. Web: www.liv.ac.uk/cmit

<sup>‡</sup>Radiology Department, Royal Liverpool University Hospitals, Prescot Street, Liverpool L7 8XP, United Kingdom.

The early variational segmentation techniques for global segmentation can be subdivided into two major categories: the edge detector based contour methods [6, 5, 12, 13, 14, 27, 32] and the region based methods [7, 8, 9, 18, 37, 43, 48, 52]. The general edge-based active contour model based on energy minimization, first proposed in 1998 by [32], detects an image contour and is later generalized to 3D segmentation by [50]; for similar works refer to [21, 49]. A major disadvantage is the inflexibility to handle changes in the topology of evolving contours during the deformation. Overcoming these drawbacks, some improved edge-based geodesic models are proposed in [13, 39, 14, 23, 54, 22].

The Mumford and Shah [43] (M-S) model provides the most influential region based method for global segmentation but it cannot be implemented directly and generally. Ambrosio and Tortorelli [4] approximated the M-S method and provided a more solvable model. Shen [46] studied a special case of [4]. Further studies [16, 38, 31] enhanced the M-S model to segment images with textures and strong noise. The Chan and Vese [18] method (C-V) is a special and effective implementation of the M-S model, making use of a level set function for the case of two phases with two approximating piecewise constants. This paper will propose a model closely related to C-V. Refer also to [18, 51]. Vese and Chan [17] extended the C-V two-phase model [18] to multiphases [52]. Zhu and Yuille [56] proposed a statistical variational approach which combined the geometrical features of a snake/balloon model and the statistical techniques of region growing. The segmentation of images with intensity inhomogeneity can be found in works of [17, 51]. Another useful class of multiphase global segmentation models is the piecewise constant level method of Tai et al. [48, 28] which only needs a single level set function to represent multiple phases. While gradient descent methods have been most widely used, fast and reliable algorithms for some of these models have been proposed in [7, 8, 30, 48]. General modeling frameworks aimed to unify variational models can be found in Mory [42]. There has been a large literature on texture segmentation; see e.g. [55, 42].

However, the division of edge based and region based models is not clearly defined. In fact, various recent and interesting developments in segmentation, of mixed type, are more effective than before: edge based models making use of level set functions to handle topology changes and region based models enhanced with edge detector functions to allow more geometry control. See [34, 13].

The above models, though exciting, aim to segment all objects in an image and cannot in general segment a specific object (which is the topic of this paper). To accurately extract a single object from an image with multi-objects, this is a new segmentation task, different from the usual global segmentation. Varying the initial contour is not always a good solution. There exist some selective models for local segmentation. Lankton et al. [33] use a local ball at each point along the contour to capture local intensity variation in regions of zero level sets, operating only on local image information. Similar works are also found in [10, 24, 36, 41, 47]. Badshah and Chen [9] (BC) proposed a segmentation model based on combining geodesic active contours and global image intensity fitting

for solving the 2D selective problem, improving the work of Gout et al. [27] especially for noisy images. This BC model is effective and can detect objects correctly for segmenting a class of 2D images. Improving on the BC work, Rada and Chen [45] proposed a robust dual level set model to overcome spurious solutions for some hard examples. Although these existing models may be further refined to increase their capabilities, our preliminary tests show that a generalized 3D version of the BC model is not effective or unfeasible since the generalized model can easily detect nearby objects for some examples. The idea of this work differs from [45]. We remark that one recent trend in global segmentation is reformulation of nonconvex models (of M-S type) as convex ones [15, 11]; however the idea is not yet ready for local segmentation as it remains to address effective ways to feed local information into a convex formulation which has the same solution from any initial guess.

In this paper, we present an adaptively active surface approach to extract a single 3D object among many objects. The minimizing energy functional is based on local image features. Our model constructs a polyhedral surface as an initial solution based on the user-supplied marker sets and the surface is evolved to give the final surface of a desired object. The rest of this paper is organized as follows. In Section 2, we review a single object extraction model of Badshah and Chen [9] for 2D case, before discussion of some existing 3D image segmentation models and their limitations. In Section 3, we first present our 3D selective segmentation model to improve the directly generalized BC model. Then, we present several important components of our method. In Section 4, we present some numerical experiments to highlight the advantages and robustness of our new adaptive 3D algorithm. We conclude the study in Section 5.

## 2 Review of some existing models

To proceed, define a 3D gray level image by  $f : \Omega \rightarrow \mathbb{R}^+$ , where  $\Omega \subset \mathbb{R}^3$  is an open and bounded set. As usual we take  $\Omega = [0, a] \times [0, b] \times [0, c]$  as the image domain and assume that only a discrete sample of image  $f$  is given. Assume that  $f$  consists of piecewise smooth features and  $\Gamma$  is the desirable interface to be found which segments  $f$  by the domain partition  $\Omega = \Omega_{in} \cup \Gamma \cup \Omega_{out}$ , where  $\Omega_{in}$  and  $\Omega_{out}$  denote inner and outer region of interface  $\Gamma$  respectively. The zero level set of a sign distance function  $\phi$  is used to represent the interface  $\Gamma$ , i.e,  $\Gamma = \{x \in \Omega : \phi(x) = 0\}$ , therefore  $\Omega_{in} = \{x \in \Omega : \phi(x) > 0\}$  can be specified by the following approximation of the  $\epsilon$ -smoothed Heaviside function:

$$H_\epsilon(\phi) = \frac{1}{2} \left( 1 + \frac{2}{\pi} \arctan(\pi\phi/\epsilon) \right)$$

and, similarly,  $\Omega_{out} = \{x \in \Omega : \phi(x) < 0\}$  is defined by  $1 - H_\epsilon(\phi(x))$ ; the derivative of  $H_\epsilon(\phi)$  is a smoothed version of the Dirac delta as follows:

$$H'_\epsilon(\phi) = \delta_\epsilon(\phi) = \frac{\epsilon}{\phi^2 + \epsilon^2}.$$

## 2.1 The BC model [9] for 2D selective segmentation

We now introduce the BC model of [9] for 2D image selective segmentation as we shall use it as a basis for building our 3D model later. The minimizing functional of the model has two kinds of terms: the regularization term and the fitting terms, as with the Chan and Vese [18] method.

Firstly for the regularization term, following [27] and the idea of geodesic active contours, the length of  $\Gamma$  is weighted by the product of an edge detector function  $g(x)$  and a distance function  $d(x)$ . A typical choice [27, 9] for  $g(x)$  is the

$$g(x) = \frac{1}{1 + a|\nabla f(x)|^2}, \quad a > 0,$$

but there also exist other variants: Chan et al. [16] choose  $g(x) = \exp(-b|\nabla f(x)|^s)$ ,  $b > 0, s > 0$  as the edge detector and Kass et al. [32] take  $g(x) = -|\nabla f(x)|^2$ . In order to deal with image noise,  $\nabla f(x)$  shall be replaced by a smoothed version  $\nabla f_\sigma$ . With these functions, the curve will locate on high values of the gradient, corresponding to the edge of a given image. Note that the gradient modulus  $|\nabla f(x)|$  of image  $f(x)$  is large at an edge pixel where we desire  $g(x) \approx 0$  or is small. At non-edge pixels,  $|\nabla f(x)| = 0$  or is small so we desire  $g(x)$  to be large (up to 1); see [13, 9, 16, 27]. Next we define the distance function  $d(x)$ . Let  $\mathcal{A} = \{x_i : i = 1 \dots n_p\}$  be a marker set which is given on boundary or near the desirable object in the given image  $f(x)$ . As in [27], Badshah and Chen [9] choose the following distance function:

$$d(x) = \prod_{i=1}^{n_p} \left(1 - \exp\left(-\frac{|x - x_i|^2}{2\sigma^2}\right)\right)$$

where  $\sigma = 4$  or  $\sigma = 3$ ; another distance function could be

$$d_2(x) = \frac{\min_{x_i \in \mathcal{A}} |x - x_i|}{\max_{x_i \in \mathcal{A}} \max_{\bar{x} \in \Omega} |\bar{x} - x_i|} = \frac{1}{M} \min_{x_i \in \mathcal{A}} |x - x_i|.$$

Note that  $d(x)$  is small near  $\mathcal{A}$ , and large away from it.

Secondly for the fitting terms, the BC model [9] adopts the Chan-Vese [18] idea for image intensities fitting, minimizing variations of intensity from the average  $C_1$  in the inside domain  $\Omega_{in}$  of an evolving curve and from the average  $C_2$  in the outside domain  $\Omega_{out}$ .

Finally the BC model takes the following form

$$\begin{aligned} \min_{\Gamma, C_1, C_2} \left\{ E(\Gamma, C_1, C_2) = \alpha E_G(\Gamma, C_1, C_2) + E_{F_1}(C_1, C_2) \right. \\ \left. = \alpha \int_{\Gamma} d(x)g(x)ds + \left[ \lambda_1 \int_{\Omega_{in}} |f(x) - C_1|^2 dx + \lambda_2 \int_{\Omega_{out}} |f(x) - C_2|^2 dx \right] \right\}. \end{aligned} \quad (1)$$

Using the level set formulation, its evolving equation can be written as

$$\frac{\partial \phi}{\partial t} = \delta_\epsilon(\phi) \left( \alpha \nabla \cdot \left( d(x)g(x) \frac{\nabla \phi}{|\nabla \phi|} \right) + \lambda_1 (f(x) - C_1)^2 - \lambda_2 (f(x) - C_2)^2 \right).$$

Actually if  $d = 1$ , the model will reduce to [35] for global segmentation, while if  $dg \approx 1$ , the model will reduce to the C-V model [18]. In fact, it is these strong connections with the global models that make the BC model detect spurious objects in some examples.

## 2.2 Some 3D global segmentation models

Although the above model will be based to propose our new 3D model shortly, there exist several 3D models for global segmentations that might be adapted for 3D selective segmentation. Below we briefly review three of such models for completeness.

### 1). Deformable surface model: TWK88 [50]

The 3D extension of the basic 2D snakes, known as the deformable surface model, was introduced by Terzopoulos et al.[50]. It was improved and applied by many others (e.g., [21, 49]). In the 3D case, a parameterized surface  $v(r, s) = (x_1(r, s), x_2(r, s), x_3(r, s))$ ,  $(r, s) \in [0, 1]^2$ , is considered, and the energy functional is given by

$$E(v) = \int_0^1 \int_0^1 \left[ \omega_{10} \left| \frac{\partial v}{\partial r} \right|^2 + \omega_{01} \left| \frac{\partial v}{\partial s} \right|^2 + \omega_{11} \left| \frac{\partial^2 v}{\partial r \partial s} \right|^2 + \omega_{20} \left| \frac{\partial^2 v}{\partial r^2} \right|^2 + \omega_{02} \left| \frac{\partial^2 v}{\partial s^2} \right|^2 + P \right] ds dr$$

where  $P = P(v) = |\nabla(G_\sigma * f(v))|$  is a generalized potential function defined by a Gaussian smoothing filter. The model is simple to use but the linearity of the *snake* model causes different parameterizations of the same initial surface to converge to different minimizers. This undesired property is the outcome of the fact that the snake model minimizes a non-geometric measure [29].

### 2). Minimal surface model: CK97 [14, 39]

The 3D intrinsic deformable models [14, 39] generalized from 2D segmentation [12] deform surfaces smoothly towards the objects in the image. Their weighted surface area geodesic active surface model is as follows

$$\min_{\Gamma} A_R = \iint_{\Gamma} g(x) dS$$

where  $dS$  is the Euclidean area element. In order to prevent the curve from shrinking to a point, a "balloon force" term (as first used by Cohen [22]) is added. Further work in a narrow band implementation can be found in [26, 25, 20].

### 3). Piecewise constant M-S 3D model: C-V [19]

The generalized 3D formulation of the 2D active contour model without edges model by [18, 19] is the following

$$\begin{aligned} \min_{\Gamma, C_1, C_2} E_\epsilon(\Gamma, C_1, C_2) = & \left\{ \gamma \int_{\Gamma} dS + \lambda_1 \int_{\Omega_{in}} |f(x_1, x_2, x_3) - C_1|^2 dx_1 dx_2 dx_3 \right. \\ & \left. + \lambda_2 \int_{\Omega_{out}} |f(x_1, x_2, x_3) - C_2|^2 dx_1 dx_2 dx_3 \right\}. \end{aligned}$$

where  $\Gamma$  is the surface separating datum  $f$  to interior and exterior of  $\Gamma$ , and  $dS$  measures the area of the separating surface, and  $\int_{\Gamma} dS$  is a regularizer that determines smoothing of the solution surface.

However, since the aim of the above global models is to segment all objects from a given datum, adapting them for local segmentation will not work in general. Our concern here is the functionality of selectivity, i.e. the detection of the single desired object which is discussed next.

### 3 A new algorithm with adaptive local fitting

To overcome the inability of the BC [9] model to stop reliably on the exact boundary of an interested object, our new idea is to use local fitting energies, i.e. to replace the fitting energy defined in the domain  $\Omega$  to a small sub-domain near the intended object. Similar use of local intensities information can be found in several recent works [41, 33]. However simply replacing the global fitting of the BC model [9] by local fitting does not lead to a satisfactory method as the band parameter is sensitive. Below we first show what form the new model takes and then discuss ways to turn it to a robust model.

Assume that a 3D image  $f(x) = f(x_1, x_2, x_3)$  is given in the cube  $\Omega \in \mathbb{R}^3$  and the set of markers, as in the 2D case (1), are defined by  $\mathcal{A} = \{x_i : i = 1 \dots n_p\}$ . Within the cubic domain  $\Omega$ , we assume these marker points are specified on three planes perpendicular to the  $x_3$  axis, as illustrated in Fig.13(a).

Our new local segmentation model is the following

$$\min_{\Gamma, C_1, C_2} \left\{ E(\Gamma, C_1, C_2) = \alpha E_G(\Gamma) + E_F(\Gamma, C_1, C_2) \right\} \quad (2)$$

where  $E_G(\Gamma) = \int_{\Gamma} G(x) ds$  is the same as (1) with  $G(x) = g(x)d(x)$ , and the new local fitting energy  $E_F(\Gamma, C_1, C_2)$  is

$$\left\{ \lambda_1 \int_{\Omega_{in}(\Gamma)} b_1(\phi(x), \gamma_{in})(f(x) - C_1)^2 dx + \lambda_2 \int_{\Omega_{out}(\Gamma)} b_2(\phi(x), \gamma_{out})(f(x) - C_2)^2 dx \right\},$$

where  $b_1(\phi(x), \gamma_{in}) = B(\phi(x), \gamma_{in}, 0)$  and  $b_2(\phi(x), \gamma_{out}) = B(\phi(x), 0, \gamma_{out})$  with

$$B(\phi(x), \gamma_{in}, \gamma_{out}) = H(\phi(x) + \gamma_{in})(1 - H(\phi(x) - \gamma_{out})) \quad (3)$$

characterizing the narrow band domain  $\Omega_{\gamma_{in}, \gamma_{out}} = \{x \in \Omega : -\gamma_{in} \leq \phi(x) \leq \gamma_{out}\} = \Omega_{\gamma_{in}}(\Gamma) \cup \Gamma \cup \Omega_{\gamma_{out}}(\Gamma)$  which is a narrow band region surrounding the local boundary  $\Gamma$  (as illustrated in Fig.1). Here we assume that  $\phi$  is negative inside  $\Gamma$  and positive outside it.

From the properties of function  $\phi(x)$ , the above optimization problem is rewritten as:

$$\min_{\phi, C_1, C_2} \alpha \int_{\Omega} G(x) |\nabla H(\phi)| dx + \int_{\Omega} \left[ \lambda_1 (1 - H(\phi)) b_1(\phi(x), \gamma_{in})(f(x) - C_1)^2 \right. \quad (4)$$

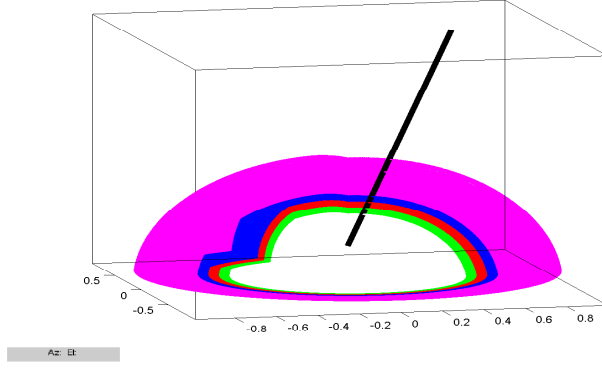


Figure 1: Illustration of two sub-domains making up the narrow band domain  $\Omega_{\gamma_{in}, \gamma_{out}}$ .

$$+ \lambda_2 H(\phi) b_2(\phi(x), \gamma_{out}) (f(x) - C_2)^2 dx$$

where we note that  $(1-H(\phi))b_1(\phi(x), \gamma_{in}) = B(\phi(x), \gamma_{in}, 0)$  and  $H(\phi)b_2(\phi(x), \gamma_{out}) = B(\phi(x), 0, \gamma_{out})$ . Further when the level set function  $\phi$  is fixed, the local mean intensities values  $C_1, C_2$  inside and outside regions of previous zero level are given by:

$$C_1 = \frac{\int_{\Omega} (1-H(\phi)) b_1(\phi(x), \gamma_{in}) f(x) dx}{\int_{\Omega} (1-H(\phi)) b_1(\phi(x), \gamma_{in}) dx}, \quad C_2 = \frac{\int_{\Omega} H(\phi) b_2(\phi(x), \gamma_{out}) f(x) dx}{\int_{\Omega} H(\phi) b_2(\phi(x), \gamma_{out}) dx} \quad (5)$$

and if  $C_1, C_2$  are fixed, we deduce the following Euler-Lagrange equation with  $G(x) \frac{\delta_{\epsilon}(\phi)}{|\nabla\phi|} \frac{\partial\phi}{\partial n} \Big|_{\partial\Omega} = 0$

$$\begin{aligned} \mathcal{N}(\phi) = & -\alpha \delta_{\epsilon} \nabla \cdot \left( G(x) \frac{\nabla\phi}{|\nabla\phi|} \right) - \lambda_1 \left[ \delta_{\epsilon}(\phi) b_1(\phi, \gamma_{in}) - (1-H(\phi)) \frac{\partial b_1(\phi, \gamma_{in})}{\partial\phi} \right] (f - C_1)^2 \\ & + \lambda_2 \left[ \delta_{\epsilon}(\phi) b_2(\phi, \gamma_{out}) + \frac{\partial b_2(\phi, \gamma_{out})}{\partial\phi} H(\phi) \right] (f - C_2)^2 = 0. \end{aligned} \quad (6)$$

The above PDE, which may be discretized by the finite difference method on a uniform mesh once a discrete image  $f$  is given, may be considered as the steady state form of the following evolution equation:

$$\frac{\partial\phi}{\partial t} = \mathcal{N}(\phi) \quad (7)$$

which is solvable by a gradient descent method in a small sub-domain (much smaller than  $\Omega$ ). Our strategy is to solve (6) directly by a multigrid method, using (7) as a smoother. We remark that the fast sweeping method [40, 1, 2] may also be used for solving (6). Though the efficiency is comparable, our method can provide better smoothing around the zero level set and hence is preferred.

Next we shall discuss some issues of implementation before we present the final algorithm. The local model will be initialized to evolve near the given marker set  $\mathcal{A}$ . We can use the set  $\mathcal{A}$  to generate a cylinder (or cuboid) like shape (as in Fig.13(c)), following Appendix 1.

### 3.1 Re-initialization

In a level set method, the interface  $\Gamma(t) = \{x \in \Omega : \phi(x, t) = 0\}$  represented implicitly by the zero level set of a function  $\phi(x, t)$  is properly evolved but outside  $\Gamma$  the level set function may become distorted. One commonly used method to scale  $\phi$  is to re-initialize it as a signed distance function which satisfies  $|\nabla\phi| = 1$ , with different signs at the two sides of the interface, often through adding  $(|\nabla\phi| - 1)^2$  to the energy functional [35].

As our main model uses local information, updating  $\phi(x, t)$  will be only carried out in a banded region for efficiency. Therefore, reinitializing it as a signed distance function is also done locally. Also,  $|\phi(x)|$  gives the (shortest) distance from  $x$  to the boundary  $\Gamma = \{x \in \Omega : \phi(x) = 0\}$ . We therefore try to keep  $\phi$  close to a signed distance function, by frequent re-initializations. Osher et al. [44] suggested solving the reinitialization equation  $\phi_t + \text{sign}(\phi)F(\phi) = 0$  where

$$F(\phi) = |\nabla\phi| - 1 \quad (8)$$

for a short period of time (i.e. practically a few time steps only).

Here we propose to solve directly  $F(\phi) = 0$ . Specifically reinitialize  $\phi$  in a local and closed domain enclosing the object to be detected by the following via a fast multigrid algorithm

$$\hat{F}(\phi) \equiv \left( \sum_{s=1}^3 [(\max(D_{x_s}^- \phi, 0))^2 + \min(D_{x_s}^+ \phi, 0)^2] \right)^{\frac{1}{2}} - 1 = 0$$

where

$$\begin{aligned} D_{x_1}^- \phi_{ijk} &= \frac{\phi_{ijk} - \phi_{i-1,jk}}{h_1}, & D_{x_1}^+ \phi_{ijk} &= \frac{\phi_{i+1,jk} - \phi_{ijk}}{h_1}; \\ D_{x_2}^- \phi_{ijk} &= \frac{\phi_{ijk} - \phi_{ij-1,k}}{h_2}, & D_{x_2}^+ \phi_{ijk} &= \frac{\phi_{ij+1,k} - \phi_{ijk}}{h_2}; \\ D_{x_3}^- \phi_{ijk} &= \frac{\phi_{ijk} - \phi_{ijk-1}}{h_3}, & D_{x_3}^+ \phi_{ijk} &= \frac{\phi_{ijk+1} - \phi_{ijk}}{h_3}. \end{aligned}$$

In 3D, developing a multigrid algorithm in a banded region (non-cuboid) is not convenient so we shall embed the interested banded region into a cuboid region. At each time  $t_n$ , this local cuboid is up to  $\gamma_{max}$  away from  $\Gamma(t_n)$  and embeds the inner part of the evolving curve  $\Gamma(t_n)$  in time step  $t_n$ ,  $\Omega_{t_n}^- = \{x = (x_i)_{i=1}^3 \in \Omega : \phi(x, t_n) < 0\}$ . First, the smallest cuboid that contains  $\Omega_{t_n}^-$  is bounded by these lower and upper bounds:  $\check{x}_{t_n,i} = \min_{x \in \Omega_{t_n}^-} x_i$ ,  $\hat{x}_{t_n,i} = \max_{x \in \Omega_{t_n}^-} x_i$  for all  $i = 1, 2, 3$ . Second, to enlarge this cuboid to a larger one that is up to  $\gamma_{max}$  away while remained in the image domain  $\Omega$ , we use the new and refined bounds:

$$\begin{aligned} \check{X}_{t_n,i} &= \begin{cases} \check{x}_{t_n,i} - \gamma_{max}, & \text{if } \check{x}_{t_n,i} - \gamma_{max} > 1; \\ 1, & \text{otherwise,} \end{cases} \\ \hat{X}_{t_n,i} &= \begin{cases} \hat{x}_{t_n,i} + \gamma_{max}, & \text{if } \hat{x}_{t_n,i} + \gamma_{max} < N_i; \\ N_i, & \text{otherwise.} \end{cases} \end{aligned}$$

Here for  $i = 1, 2, 3$ , let  $I_{t_n, i} = [\check{X}_{t_n, i}, \hat{X}_{t_n, i}]$  denote the sub-interval along  $x_i$ -direction at  $t_n$  step. Then a multigrid algorithm will be applied to solve the static Hamilton-Jacobi equation  $F(\phi) = 0$  (see (8)) in the cuboid:  $\Omega_{t_n}^L = I_{t_n, 1} \times I_{t_n, 2} \times I_{t_n, 3} \subset \Omega$  such that  $\Omega_{t_n}^L = (\Omega_{t_n}^L)^- \cup \Gamma(t_n) \cup (\Omega_{t_n}^L)^+$  with  $\Gamma_{t_n} = \{x \in \Omega : \phi(x, t_n) = 0\}$ ,  $(\Omega_{t_n}^L)^- = \{x \in \Omega_{t_n}^L : \phi(x, t_n) < 0\} = \Omega_{t_n}^-$  inside of  $\Gamma(t_n)$ , and  $(\Omega_{t_n}^L)^+ = \{x \in \Omega_{t_n}^L : \phi(x, t_n) > 0\} \subset \Omega_{t_n}^+$  outside of  $\Gamma(t_n)$ .

**Reinitialization based on a multigrid method.** The finest grid, denoted by  $G(1)$ , will have  $N_{t_n, 1}^L \times N_{t_n, 2}^L \times N_{t_n, 3}^L$  uniformly distributed voxel grid points where  $N_{t_n, i}^L = \hat{X}_{t_n, i} - \check{X}_{t_n, i} + 1 = p_{t_n, i} \cdot 2^{q_{t_n, i}} + 1$ , with  $p_{t_n, i}$  ( $n = 1, 2, \dots$  and  $i = 1, 2, 3$ ) integers greater than 1 and  $q_{t_n, i}$  ( $n = 1, 2, \dots$  and  $i = 1, 2, 3$ ) nonnegative integers. In this work, standard grid coarsening is implemented [3], with the local cuboid  $\Omega_{t_n}^L$  covered by  $\ell_{t_n} = \max_{1 \leq s \leq 3} q_{t_n, s} + 1$  grids:  $G(1), G(2), \dots, G(\ell_{t_n})$  with  $G(1)$  the finest and  $G(\ell_{t_n})$  the coarsest with  $(p_{t_n, 1} + 1) \times (p_{t_n, 2} + 1) \times (p_{t_n, 3} + 1)$  grid points.

In addition to restriction and interpolation operators, a multigrid method solving the discrete system (8) requires a suitable smoother based on some iterative relaxation method which is often the decisive factor in determining whether or not a multigrid algorithm converges. Here we use a time-marching scheme as the smoother:

$$\phi^{n+1} = \phi^n + \Delta t \left\{ [\max(\text{sign}(\phi^0), 0) \nabla^{(+)} + \min(\text{sign}(\phi^0), 0) \nabla^{(-)}] \phi^n \right\}$$

where

$$\begin{aligned} \nabla^{(-)} \phi^n &= \left\{ \sum_{s=1}^3 \left( [\max(D_{x_s}^{(+)} \phi^n, 0)]^2 + [\min(D_{x_s}^{(-)} \phi^n, 0)]^2 \right) \right\}^{\frac{1}{2}}; \\ \nabla^{(+)} \phi^n &= \left\{ \sum_{s=1}^3 \left( [\max(D_{x_s}^{(-)} \phi^n, 0)]^2 + [\min(D_{x_s}^{(+)} \phi^n, 0)]^2 \right) \right\}^{\frac{1}{2}}. \end{aligned}$$

### 3.2 Adaptive update of localizing parameters $\gamma_{in}$ and $\gamma_{out}$

As mentioned above, the local functional  $b_i(\phi, \gamma)$ ,  $i = 1, 2$ , in our main energy functional  $E(\phi, C_1, C_2)$  has a localizing parameter  $\gamma$  (on either side of the evolving surface) which is crucial to the success of the model. A fixed parameter  $\gamma$  does not lead to a robust method. If  $\gamma$  is too small, the model captures less image features and the surface might even stop evolving before reaching the object boundary, or conversely if  $\gamma$  is too large, the active surface is likely to detect other objects (i.e. fail the model).

We propose to vary  $\gamma$  and optimize it for the given image  $f$ . The central question is how to select  $\gamma$  automatically, at each iteration, because it is in general unknown *a priori*. The clue lies in the fact that intensity variations within inner and outer narrow regions are approximately zero when the zero level curve stops on the object boundary. This observation can be explored by varying the band widths in an interval in order to find the optimized width that helps reducing such intensity variations. This

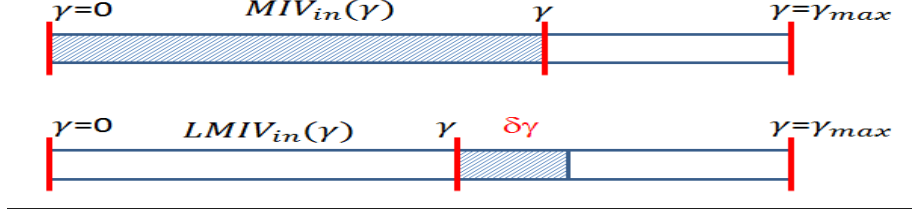


Figure 2: Illustration of computing variations for band width selection.

locally optimal band width leads to our variable- $\gamma$  method. Therefore our basic idea for finding the optimal  $\gamma$  automatically is to select from the extremal points of a mean intensity variation function and a local mean intensity variation function with respect to the localizing parameter  $\gamma$  surrounding the zero level curve.

We first consider the selection of  $\gamma = \gamma_{in}$ , in a three-stage procedure. Note, from (3),  $[1 - H(\phi)]H(\phi + \gamma_{in}) = [1 - H(\phi)]b_1(\phi, \gamma_{in}) = B(\phi(x), \gamma_{in}, 0)$  characterizes the inner band domain  $\Omega_{in}(\Gamma)$ .

**Stage 1** — Movement towards the object, where image intensities change the most or the least. Define a mean intensities variations function  $MIV_{in}(\gamma)$  by

$$MIV_{in}(\gamma) = \left\{ \frac{\int_{\Omega} [1 - H(\phi)]H(\phi + \gamma)[f(x) - MI_{in}(\gamma)]^2 dx}{\int_{\Omega} [1 - H(\phi)]H(\phi + \gamma) dx} \right\}^{\frac{1}{2}}$$

where  $MI_{in}(\gamma)$  is the mean intensity (MI) given by

$$MI_{in}(\gamma) = \frac{I_{in}(\gamma)}{\int_{\Omega} [1 - H(\phi)]b_1(\phi, \gamma) dx}, \quad I_{in}(\gamma) = \int_{\Omega} [1 - H(\phi)]b_1(\phi, \gamma)f(x) dx.$$

See the top plot of Fig.2 for illustration. Then the first extremal point  $\gamma$  in  $MIV_{in}(\gamma)$  will be our most profitable parameter, provided that it is not  $\gamma_{max}$ . Formally, our optimal parameter is  $\gamma^* = \min_{\gamma} \Theta_{in}$  if  $\gamma^* \neq \gamma_{max}$ , where the extremal point set of  $MIV_{in}(\gamma)$  in  $(\gamma_{min} - 1, \gamma_{max}]$  is defined by:

$$\Theta_{in} = \left\{ \gamma : \left( \arg \max_{\gamma_{min}-1 < \gamma \leq \gamma_{max}} MIV_{in}(\gamma) \right) \cup \left( \arg \min_{\gamma_{min}-1 < \gamma \leq \gamma_{max}} MIV_{in}(\gamma) \right) \right\}.$$

**Stage 2** — Movement towards the object, where incremental image intensities change the most or the least. If Stage 1 is already successful, we consider Stage 3 next. If not, i.e.  $\min_{\gamma} \Theta_{in} = \gamma_{max}$ , we consider the local mean intensity variation function  $LMIV_{in}(\gamma)$  within  $\delta\gamma$  band strip (as illustrated in bottom plot of Fig.2). For a fixed  $\delta\gamma > 0$ , the quantity  $[1 - H(\phi)][H(\phi + \gamma + \delta\gamma) - H(\phi + \gamma)]$  defines the narrow strip of width  $\delta\gamma$  near the narrow band  $\gamma$ . We define  $LMIV_{in}(\gamma)$  by

$$LMIV_{in}(\gamma) = \left\{ \frac{\int_{\Omega} [1 - H(\phi)][H(\phi + \gamma + \delta\gamma) - H(\phi + \gamma)][f(x) - LMI_{in}(\gamma, \delta\gamma)]^2 dx}{\int_{\Omega} [1 - H(\phi)][H(\phi + \gamma + \delta\gamma) - H(\phi + \gamma)] dx} \right\}^{\frac{1}{2}}$$

where  $LMI_{in}(\gamma)$  is the mean intensity of  $f$  in  $\delta\gamma$  band strip at  $\gamma$ :

$$LMI_{in}(\gamma) = \frac{I_{in}(\gamma + \delta\gamma) - I_{in}(\gamma)}{\int_{\Omega} [1 - H(\phi)][H(\phi + \gamma + \delta\gamma) - H(\phi + \gamma)] dx}.$$

Our optimal parameter  $\gamma^*$  is taken as  $\gamma^* = \min_{\gamma} \Xi_{in}$  where

$$\Xi_{in} = \left\{ \gamma : \left( \arg \max_{\gamma_{min}-1 < \gamma \leq \gamma_{max}} LMIV_{in}(\gamma) \right) \cup \left( \arg \min_{\gamma_{min}-1 < \gamma \leq \gamma_{max}} LMIV_{in}(\gamma) \right) \right\}.$$

Overall, from Stages 1-2, we select our localizing parameter  $\gamma_{in}$  by

$$\gamma_{in} = \begin{cases} \min_{\gamma} \Theta_{in}, & \text{if } \min_{\gamma} \Theta_{in} < \gamma_{max}; \\ \min_{\gamma} \Xi_{in}, & \text{otherwise.} \end{cases} \quad (9)$$

Analogously, we choose the outer parameter  $\gamma_{out}$  via these quantities

$$\begin{aligned} I_{out}(\gamma) &= \int_{\Omega} H(\phi)[1 - H(\phi - \gamma)]f(x)dx; & MI_{out}(\gamma) &= \frac{I_{out}(\gamma)}{\int_{\Omega} H(\phi)[1 - H(\phi - \gamma)]dx}; \\ MIV_{out}(\gamma) &= \left\{ \frac{\int_{\Omega} H(\phi)[1 - H(\phi - \gamma)](f(x) - MI_{out}(\gamma))^2 dx}{\int_{\Omega} H(\phi)[1 - H(\phi - \gamma)]dx} \right\}^{\frac{1}{2}}; \\ LMI_{out}(\gamma) &= \frac{I_{out}(\gamma + \delta\gamma) - I_{out}(\gamma)}{\int_{\Omega} H(\phi)[H(\phi - \gamma) - H(\phi - \gamma - \delta\gamma)]dx}; \\ LMIV_{out}(\gamma) &= \left\{ \frac{\int_{\Omega} H(\phi)[H(\phi - \gamma) - H(\phi - \gamma - \delta\gamma)][f(x) - LMI_{out}(\gamma, \delta\gamma)]^2 dx}{\int_{\Omega} H(\phi)[H(\phi - \gamma) - H(\phi - \gamma - \delta\gamma)]dx} \right\}^{\frac{1}{2}} \end{aligned}$$

with  $\Theta_{out}, \Xi_{out}$  similarly defined; hence the optimal  $\gamma_{out}$  is chosen as

$$\gamma_{out} = \begin{cases} \min_{\gamma} \Theta_{out}, & \text{if } \min_{\gamma} \Theta_{out} < \gamma_{max}; \\ \min_{\gamma} \Xi_{out}, & \text{otherwise.} \end{cases} \quad (10)$$

In a discrete setting, we take positive integers for  $\gamma_{in}, \gamma_{out}$  and set  $\delta\gamma = 1$ , and  $\eta_0 = 0.02$  for removing the small disturbance of  $MIV_{\iota}(\gamma)$  or  $LMIV_{\iota}(\gamma)$  (with  $\iota = \text{'in'}, \text{'out'}$ ). Then  $\Theta_{\iota}$  and  $\Xi_{\iota}$  can be simplified to the following  $\bar{\Theta}_{\iota}$  and  $\bar{\Xi}_{\iota}$  respectively:

$$\begin{aligned} \bar{\Theta}_{\iota} &= \{\gamma_{max}\} \cup \left\{ \gamma \in N : \gamma_{min} \leq \gamma \leq \gamma_{max} \text{ such that} \right. \\ &\quad MIV_{\iota}(\gamma) \leq (1 - \eta_0)MIV_{\iota}(\gamma - 1) \text{ and } MIV_{\iota}(\gamma) < (1 - \eta_0)MIV_{\iota}(\gamma + 1) \left. \right\} \\ &\quad \cup \left\{ \gamma \in N : \gamma_{min} \leq \gamma \leq \gamma_{max} \text{ such that} \right. \\ &\quad \left. MIV_{\iota}(\gamma) \geq (1 + \eta_0)MIV_{\iota}(\gamma - 1) \text{ and } MIV_{\iota}(\gamma) > (1 + \eta_0)MIV_{\iota}(\gamma + 1) \right\}; \\ \bar{\Xi}_{\iota} &= \{\gamma_{max}\} \cup \left\{ \gamma \in N : \gamma_{min} \leq \gamma \leq \gamma_{max} \text{ such that} \right. \\ &\quad LMIV_{\iota}(\gamma) \leq (1 - \eta_0)LMIV_{\iota}(\gamma - 1) \text{ and } LMIV_{\iota}(\gamma) < (1 - \eta_0)LMIV_{\iota}(\gamma + 1) \left. \right\} \\ &\quad \cup \left\{ \gamma \in N : \gamma_{min} \leq \gamma \leq \gamma_{max} \text{ such that} \right. \\ &\quad \left. LMIV_{\iota}(\gamma) \geq (1 + \eta_0)LMIV_{\iota}(\gamma - 1) \text{ and } LMIV_{\iota}(\gamma) > (1 + \eta_0)LMIV_{\iota}(\gamma + 1) \right\}. \end{aligned}$$

To alleviate the effect of image noise on  $MIV_{\iota}(\gamma)$  or  $LMIV_{\iota}(\gamma)$ , we replace absolute inequality tests by relative inequalities, e.g.,  $MIV_{\iota}(\gamma_i), MIV_{\iota}(\gamma_{i+1})$  ( or  $LMIV_{\iota}(\gamma_i), LMIV_{\iota}(\gamma_{i+1})$ ) are only compared for every minimizer/maximizer  $\gamma_i \in \bar{\Theta}_{\iota}$  (or  $\gamma_i \in \bar{\Xi}_{\iota}$ ) if

$$\begin{aligned} &|MIV_{\iota}(\gamma_i) - MIV_{\iota}(\gamma_{i+1})| \geq \eta_3 |MIV_{\iota}(\gamma_i) + MIV_{\iota}(\gamma_{i+1})|; \\ \text{or } &|LMIV_{\iota}(\gamma_i) - LMIV_{\iota}(\gamma_{i+1})| \geq \eta_3 |LMIV_{\iota}(\gamma_i) + LMIV_{\iota}(\gamma_{i+1})| \end{aligned} \quad (11)$$

for some  $0 < \eta_3 < 1$ ; otherwise the difference is small and  $\gamma_i$  is not considered as an extremal point.

**Stage 3** — Movement away from ‘homogeneous’ subregions in a fast way (i.e. using the largest band width). The above two Stages lead to optimized parameters for band widths  $\gamma_{in}$  and  $\gamma_{out}$ . One of these two parameters needs to be modified in one of the following special cases of the zero level set surface: i) it is entirely within the object; ii) it completely embeds the object. Here the latter is less likely with our initially supplied surface. Nevertheless to accelerate the surface evolving process, we propose  $\gamma_{out} = \gamma_{max}$  for i) or  $\gamma_{in} = \gamma_{max}$  for ii).

To tell if one of these two cases holds, we compare both mean intensities (i.e. MI) and mean gradients between  $\Omega_{\gamma_{in}}$  and  $\Omega_{\gamma_{out}}$ . Their mean gradients can be respectively defined by

$$MG_{in}(\gamma_{in}) = \frac{\int_{\Omega} [1 - H(\phi)] H(\phi + \gamma_{in}) |\nabla f(x)| dx}{\int_{\Omega} [1 - H(\phi)] H(\phi + \gamma_{in}) dx};$$

$$MG_{out}(\gamma_{out}) = \frac{\int_{\Omega} H(\phi) [1 - H(\phi - \gamma_{out})] |\nabla f(x)| dx}{\int_{\Omega} H(\phi) [1 - H(\phi - \gamma_{out})] dx}.$$

If  $\frac{|MI_{in}(\gamma_{in}) - MI_{out}(\gamma_{out})|}{|MI_{in}(\gamma_{in}) + MI_{out}(\gamma_{out})|} < \eta_1/2$  and  $\frac{|MG_{in}(\gamma_{in}) - MG_{out}(\gamma_{out})|}{|MG_{in}(\gamma_{in}) + MG_{out}(\gamma_{out})|} < \eta_2/2$  for some small  $\eta_1, \eta_2$  such that  $0 < \eta_1, \eta_2 < 1$ , then one of the above two cases is present. Using any initial slice where markers are specified, we can differentiate case i) from ii) by measuring and comparing the distances from such markers. This completes our selection procedure of 3 Stages.

To summarize, our proposed  $\gamma$ -choice is based on three quantities:

- the mean variations  $MIV(\gamma)$ ,
- the local mean variations  $LMIV(\gamma)$  and
- the mean gradient variations  $MG(\gamma)$ .

The procedure is illustrated for three examples in Figure.3(a)-3(c). The use of these 2D images is for visual illustration purpose as our procedure applies to 3D images. There, we set  $\gamma_{min} = 2$  and  $\gamma_{max} = 30$ , and the other parameters as follows:  $\eta_1 = 0.2$ ,  $\eta_2 = 0.2$  and  $\eta_3 = 0.1$ . Clearly the  $\gamma$ -choice is effective for moving the zero level curve in monkey image and CT image, for example in Figure.3(a)-3(c) we can see that mean variation  $MIV_{in}(\gamma)$  of inner narrow band has a minimizer  $\gamma_{in} = 5$ , while mean variation  $MIV_{out}(\gamma)$  of outer narrow band is a monotone decreasing function. So we should check the minimizers/maximizers of local mean variation  $LMIV_{out}(\gamma)$ , however the difference  $|MIV_{\ell}(\gamma_i) - MIV_{\ell}(\gamma_{i+1})|$  (or (11)) for every minimizer/maximizer  $\gamma_i < 21$  is small and such minimizer/maximizer  $\gamma_i$  is not considered as an optimal extremal point.

### 3.3 Fast solution of (7) in a sub-domain

Solution of (7) can be expensive in the whole 3D domain  $\Omega$ . If  $N$  is the number of points (pixels) in each spatial direction, and the number of voxels is  $N^3$ , the level set algorithm in solving (7) has

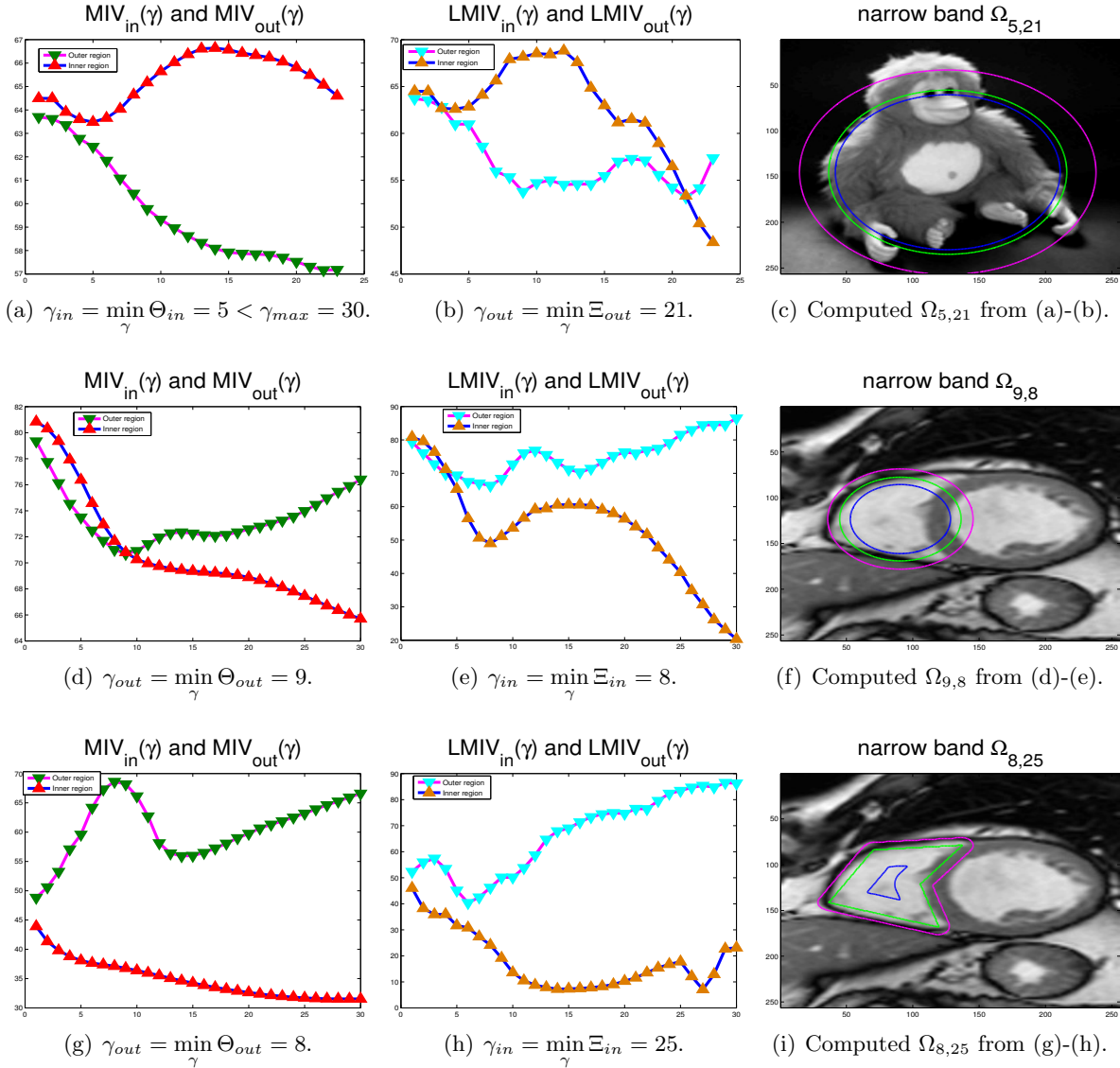


Figure 3: Choice of  $\gamma_{in}$  and  $\gamma_{out}$  by our narrow band algorithm. First column: the plots of mean variation  $MIV_{in}(\gamma)$  and  $MIV_{out}(\gamma)$  with respect to localizing parameter  $\gamma$ ; second column: The plots of local mean variation  $LMIV_{in}(\gamma)$  and  $LMIV_{out}(\gamma)$  with respect to localizing parameter  $\gamma$ ; third column: narrow band  $\Omega_{\gamma_{in},\gamma_{out}}$  between *blue* contour and *magenta* contour is captured by parameter  $\gamma_{in}$  and  $\gamma_{out}$  (computed by using (9), (10) and filter term (11)), and *green* contour is the tested zero level.

at least an  $O(N^3)$  complexity per time step. However the number of voxels in  $\Omega_{\gamma_{in}, \gamma_{out}}$  near the evolving surface is much less, roughly  $O(N^2)$ ; see Figure 1 for an illustration. As remarked in [39] and others, in a surface evolving process, we are interested in the motion of the zero-level set and not in the motion of each isophote of the surface. So we only need to compute in a cuboid containing the surface  $\Gamma(t)$ , such a technique significantly decreases the computational complexity, in particular when implemented efficiently. As remarked, the method of fast sweeping as used in [40, 1, 2] for a different model may also be applied here.

This cuboid idea is used in this work with the cuboid constructed by choosing points that lie less than some given distance away from the surface  $\Gamma(t)$  (such as  $\gamma_{in}$  and  $\gamma_{out}$  as mentioned). The resulting local domain contains the zero-level set – the active marching surface  $\Gamma(t)$ .

### 3.4 The overall numerical algorithm

Our new algorithm for solving (7) as summarized in the following Algorithm 1 has these ingredients:

- the given marker nodes on slices of a 3D datum are made full use to produce an accurate initial level set contour surface;
- optimized inner and outer band widths are found using local variations near the evolving contour surface;
- A nonlinear multigrid method using a gradient descent smoother is employed in a cuboid containing the narrow banded domain to maintain the level set function to be a signed distance function;
- The gradient gradient solution is only conducted in the narrow banded domain to give a fast implementation.

Here the first two aspects are indispensable for the success of our approach, while the last two aspects ensure a fast solution method but there exist alternative ways of implementation.

Algorithm 1 is stopped if the maximum number  $it$  of iterations is reached (usually  $it = 1000$ ), or the relative error in two consecutive iterative steps is smaller than a tolerance  $\eta_0$  (typically  $\eta_0 = 10^{-6}$  for a practical segmentation), or the number of pixels inside a zero level set is smaller than 15.

## 4 Numerical Experiments

This section presents some test results to demonstrate three points:

- effectiveness of our initial solution construction based on  $\mathcal{A}$ ;
- comparison with the BC model [9] for 3D segmentation;
- effectiveness of our new model for some complex extractions.

**Algorithm 1 (A fast surface marching algorithm)**

- step 1. Input markers set:  $\mathcal{A} = \{\bar{x}^\ell = (x_1^\ell, x_2^\ell, x_3^\ell)^T : \ell = 1, \dots, \bar{\ell}\}$ ; set  $n = 0$  and  $it = It_{in}$ .*
- step 2. Obtain the initial level set function  $\phi_0$  by our initial strategy from Appendix 1.*
- step 3. Obtain the Reinitialization sub-region  $\Omega_{t_n}^L$  from Section 3.1.*
- step 4. Reinitialization the level set function  $\phi_n$  in sub-region  $\Omega_{t_n}^L$  by multigrid.*
- step 5. Obtain inner and outer cuboid-size:  $\gamma_{in}^n$  and  $\gamma_{out}^n$  from Section 3.2.*
- step 6. Obtain local mean intensities  $C_1$  and  $C_2$  and construct the marching cuboid.*
- step 7. Solve the evolving equation in the cuboid.:*  
*-  $\phi^{n+1} = ELV\_local(\phi^n, \gamma_{in}^n, \gamma_{out}^n, \dots, It_{in})$ ;*
- step 8. Check for convergence using stopping criteria*  
*- if not satisfied; set  $n = n + 1$  and go to step 3.;*  
*- else return solution  $\phi^* = \phi^{n+1}$ .*

Both synthetic and real life medical images are chosen for our tests below. In all results, we have used the marker set  $\mathcal{A} = \{x_i = (x_i^1, x_i^2, x_i^3) : i = 1, \dots, n_p\}$  for a relatively small number  $n_p \geq 9$ , which is the sum of 3 sets of markers on three image slices only. We take the fitting weights  $\lambda_1 = \lambda_2 = 1$ , smoothing parameter  $\epsilon = 1$ , discretization scale  $h = 1$  and time step  $\tau = 0.1$ , we also set  $\gamma_{min} = 2$  and  $\gamma_{max} = 30$  as mentioned in the previous section.

**1). Tests on the initial solution strategy.** Here, we begin our numerical experiments by demonstrating the usefulness of initial evolving surfaces in Fig.13 for image selective segmentation on a synthetic 3D image in Fig.4. This synthetic image features two important challenges that can be resolved effectively by our strategy: 1) a thin separation gap, i.e., the interested object is near other objects of the same intensity; 2) a highly skewed object, i.e., the interested region is a long and flat object. Fig.4(a) shows a result with an initial contour by our strategy (Appendix 1) where the middle non-convex object is the aim of detection. Fig.4(b) shows the result of two objects within zero level of  $\phi_0$  captured by a simplex initial solution strategy. Fig.4(c) and 4(d) show their slices along  $z$ -direction, respectively. Clearly our proposed construction for the initial surface is more logical than the alternative approach.

**2). Comparisons with the Badshah-Chen model [9] in 3D.** We have explained that the Badshah-Chen model [9] has improved the geodesic model by Gout et al.[27] for noisy images, and that the model works well when the separation distance (of the interested object from other nearby objects) is large and the target feature is of a simple convex shape. We now illustrate the above remarks using two test cases as in Fig.5 and Fig.6.

First, Fig.5 shows the results for a 3D image by our proposed method; the original image with its

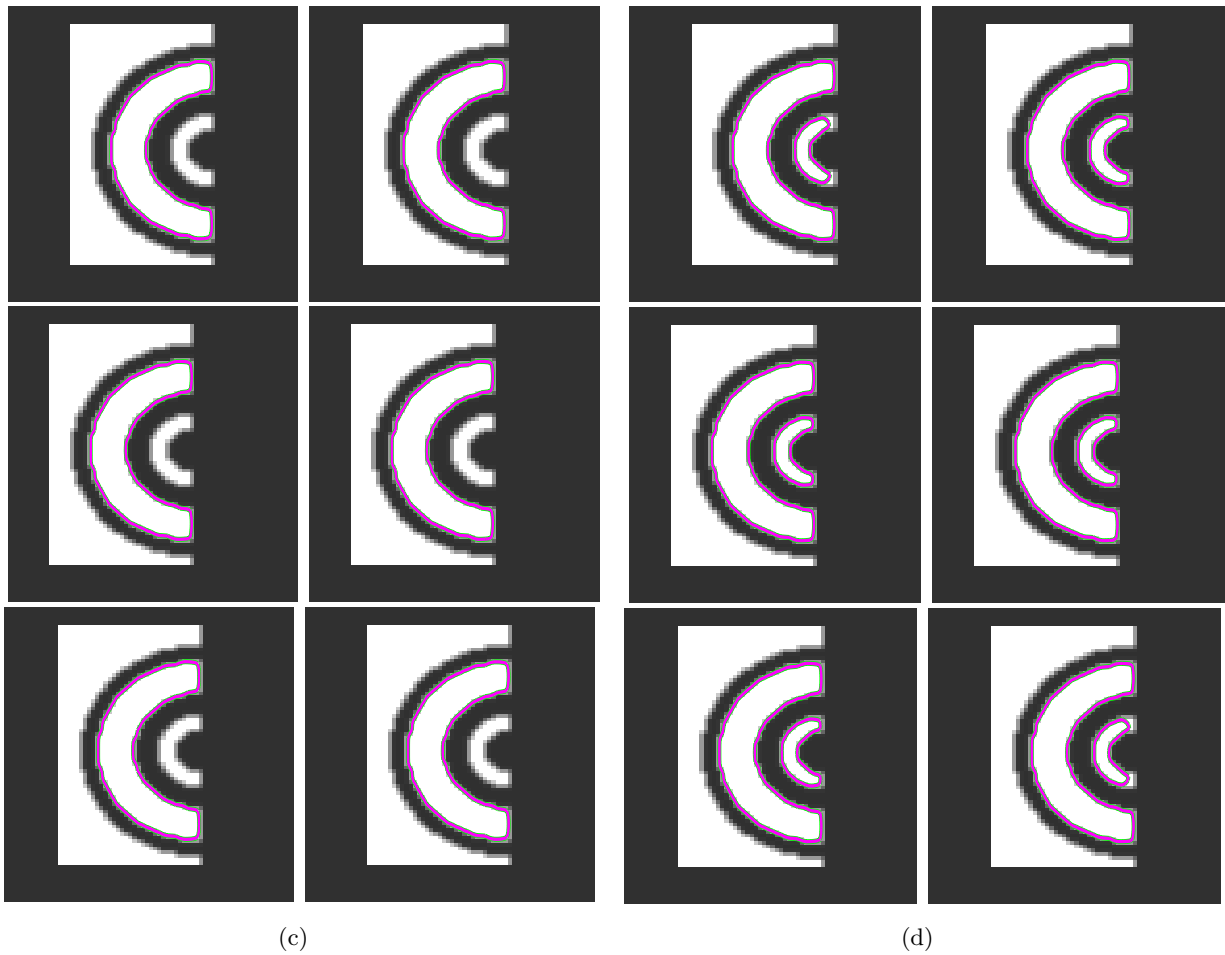
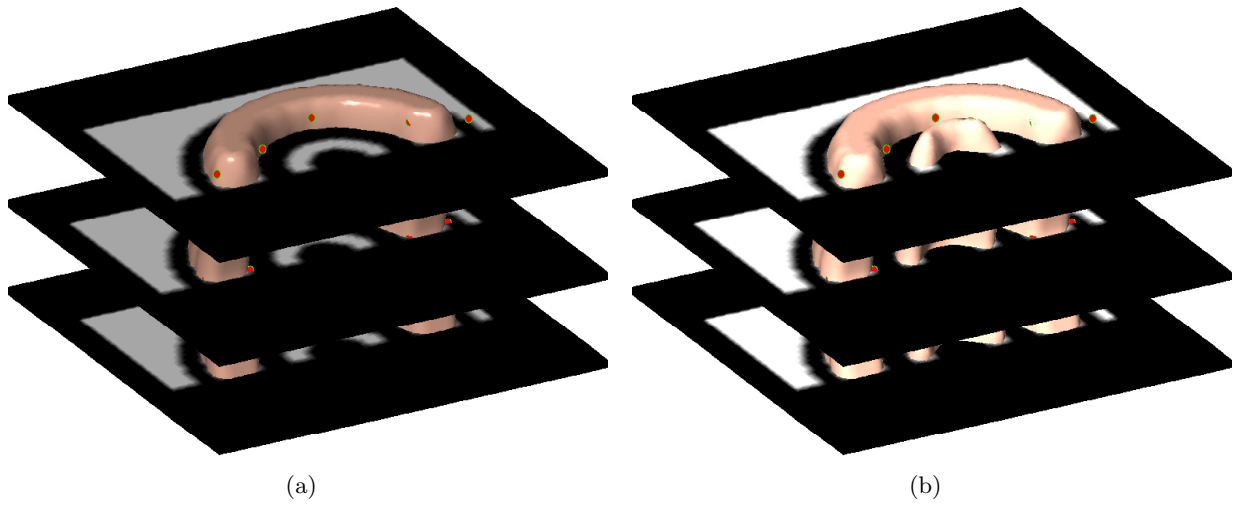


Figure 4: Comparisons for initial solution strategies. (a) Successful result by our proposed initial solution; (b) Unsuccessful result by simplex initial solution; (c)-(d) Slice-presentations of (a) and (b), respectively.

initial zero level by a polyhedral surface and markers sets are shown in Fig.5(a)-5(b) and 5(d). The successful result and some selected slices from our new method are shown in Fig.5(c) and 5(e)-5(f). In contrast, starting from the same initial guess as shown in Fig.5(a)-5(b) and 5(d), the Badshah-Chen model detects the incorrect result (evidently redundant features are extracted) shown in Fig.6. Additionally, computation time of our approach is about 20 minutes while the BC model will cost more than 2 hours on the same computer. On the whole, our method yields encouraging results.

**3). Tests for other complex extractions.** Our final two experiments are conducted on harder and more challenging medical data. Here in test 1, the interested object has a complex shape and a small separation gap: see Fig.7. Then segmentation solutions using our proposed method are shown in Fig.7(c),7(e)-7(f).

Similarly for test 2, the original and our segmented results are shown in Fig.8. Clearly our new method delivers the expected result and correctly segments the intended objects.

#### 4). RV Segmentation Challenge in Cardiac MRI from MICCAI

Although our motivation for this work comes from organ extraction problems from the local Royal Liverpool University Hospital and our developed model has been shown to be effective, it is useful to test our model on the datasets of the MICCAI Segmentation Grand Challenges. Unfortunately such datasets are not widely or publicly available and only some partial datasets are obtainable.

Nevertheless in this final test, we apply our 3D selective segmentation method to the datasets from the MICCAI 2012 Cardiac MR Right Ventricle Segmentation Challenge (RVSC)<sup>1</sup> that was set to segment the Right Ventricle for a training set and a test set, with each slice contour being represented as zero level of level set function. As we have mentioned in previous experiments, markers are placed on the third, the middle and the third from last slices (3, 5 and 3 markers respectively) to construct the original guess.

Here we compare our algorithm (3D implementation) with the manual outlining (2D slices) from RVSC in the *RSMr* (region similarity measure *ratio*) value which is defined by

$$RSMr = \frac{\#(\Omega_1^* \cap \Omega_2^*)}{\#(\Omega_2^*)}$$

and in visual quality where  $\Omega_1^*$  and  $\Omega_2^*$  are the regions extracted by our solution contours (to be called “automatic”) and manual contours (to be denoted by “manual”) in 2D slices and  $\#(U)$  denotes the number of pixels in region  $U$ . We remark that all not manual outlines are published on the MICCAI site, although the full data of RVSC are available for testing.

Firstly, our segmentation algorithm is run on the 3D image of Patient 12 (a training data set) while comparisons can only be done for manual delineations of some contours (*red* contour)

---

<sup>1</sup>MICCAI grand challenge website: [http://www.grand-challenge.org/site/grand-challenges/all\\_challenges](http://www.grand-challenge.org/site/grand-challenges/all_challenges), the authors also thank Caroline Petitjean for data downloading authorization of Test1 Set and Training Set in links: <http://www.litislab.eu/rvsc/downloadfiles/>.

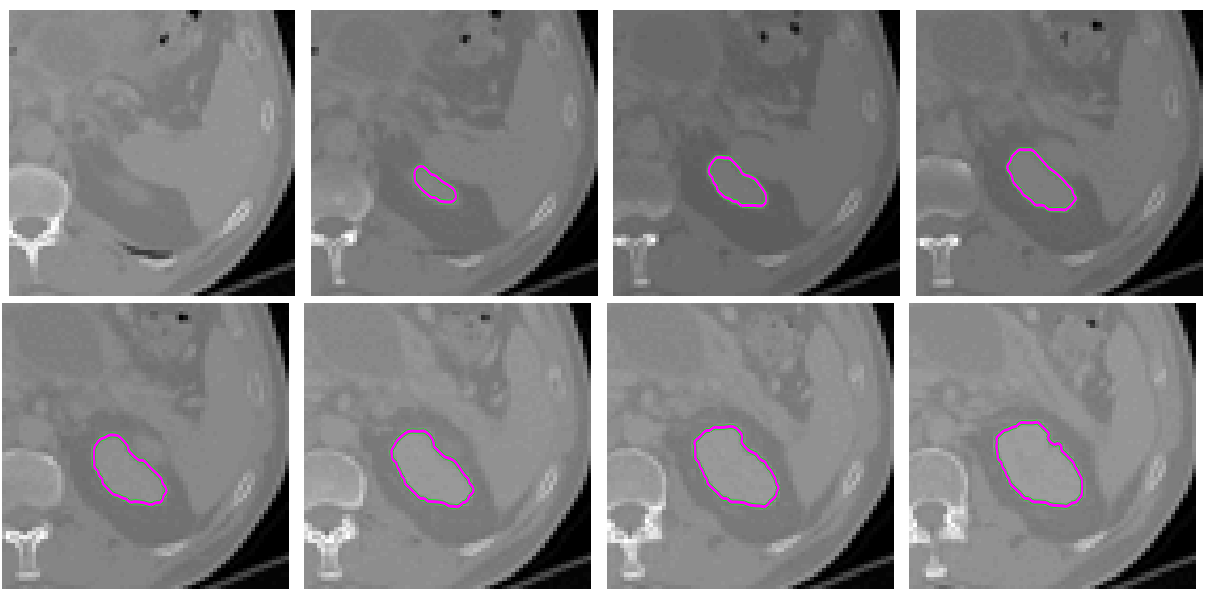
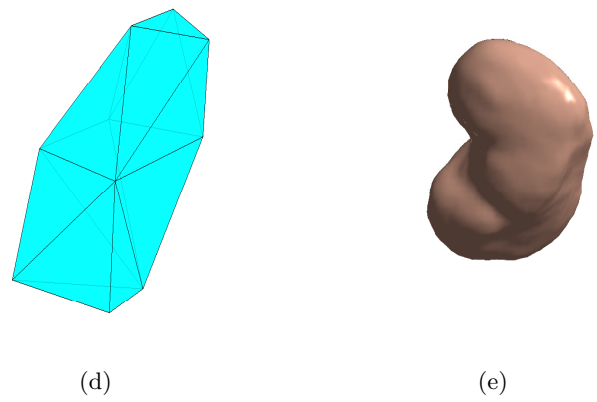
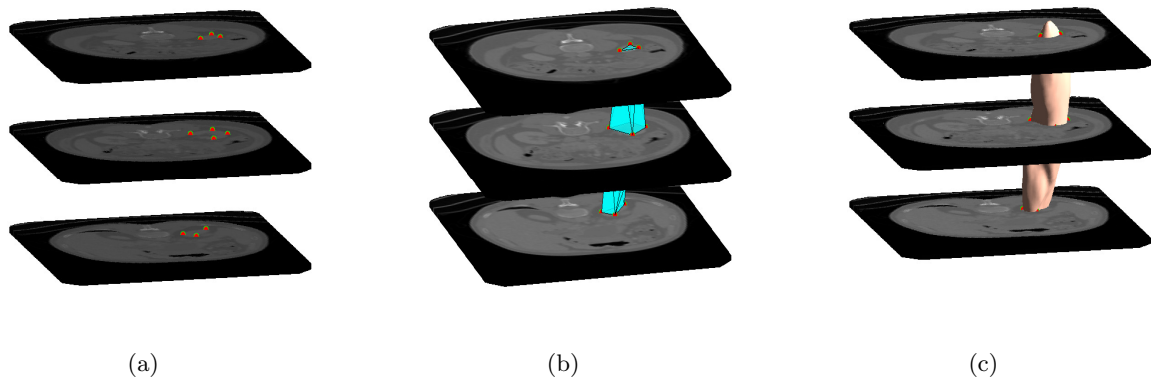
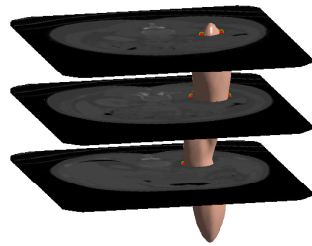


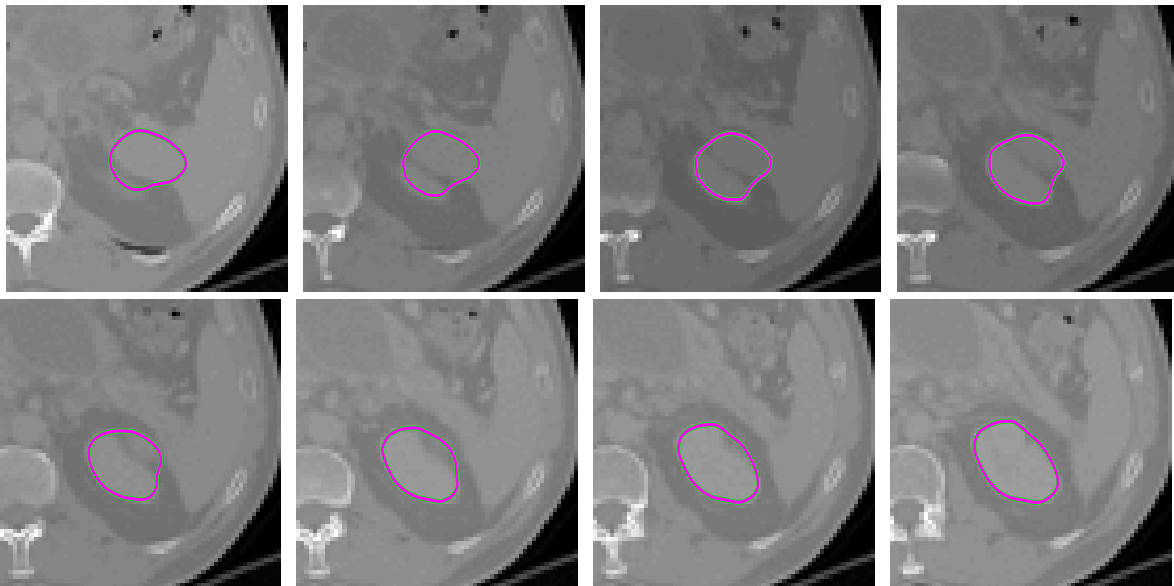
Figure 5: Comparisons with Badshah-Chen model in [9] – Part 1. (a) Original datum: slice-representation and marker sets in three slices (red dots are the markers); (b) and (d) Initial solution surface by our new strategy; (c) and (e) Successful result by our proposed method; (f) Slice-representations of (e).



(a)

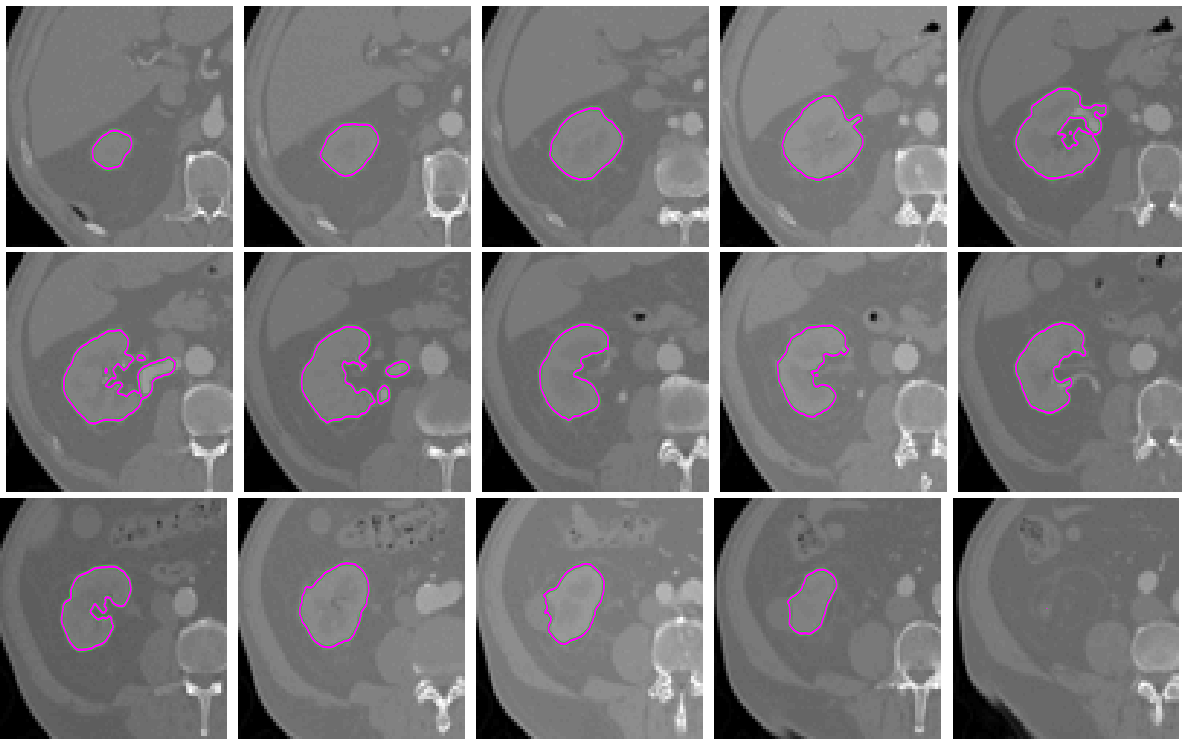
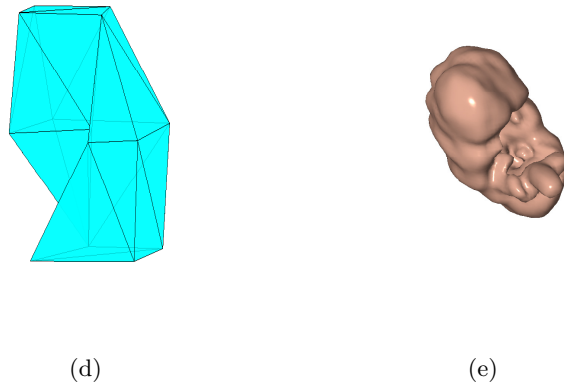
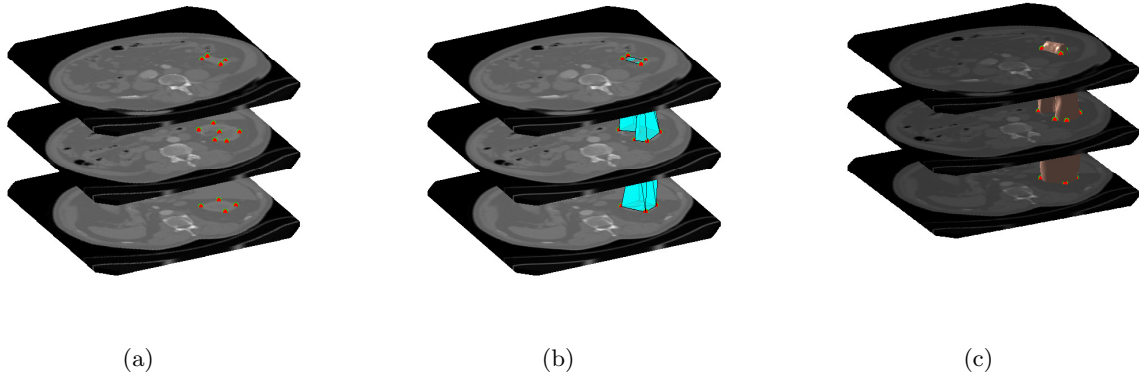


(b)



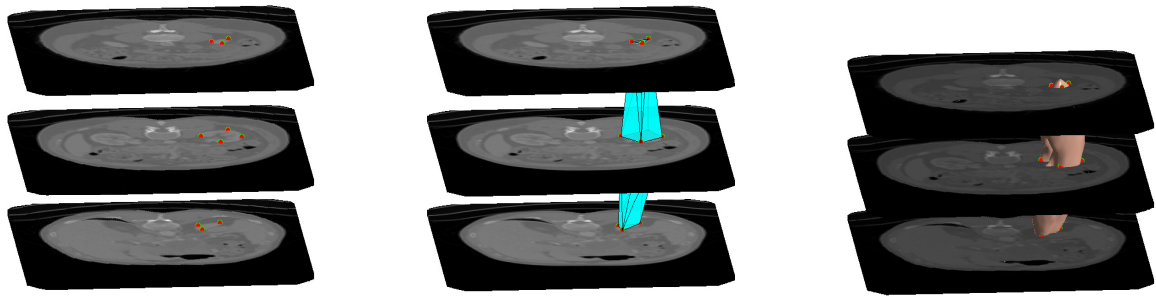
(c)

Figure 6: Comparisons with the BC model in [9] – Part 2. (a)-(b) Unsuccessful result by the BC model; (c) Slice-presentations of (b), here the same initial guess with Figure 5 is used in this model.



(f)

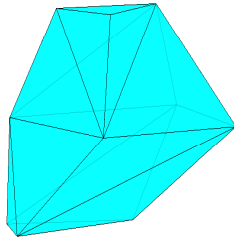
Figure 7: Test 1 for a complex shape problem. (a) Original datum: slice-representation and marker sets in three slices (red dots are the markers); (b) and (d) Initial solution surface by our new strategy; (c) and (e) Successful result by our proposed method; (f) Slice-presentations of (e).



(a)

(b)

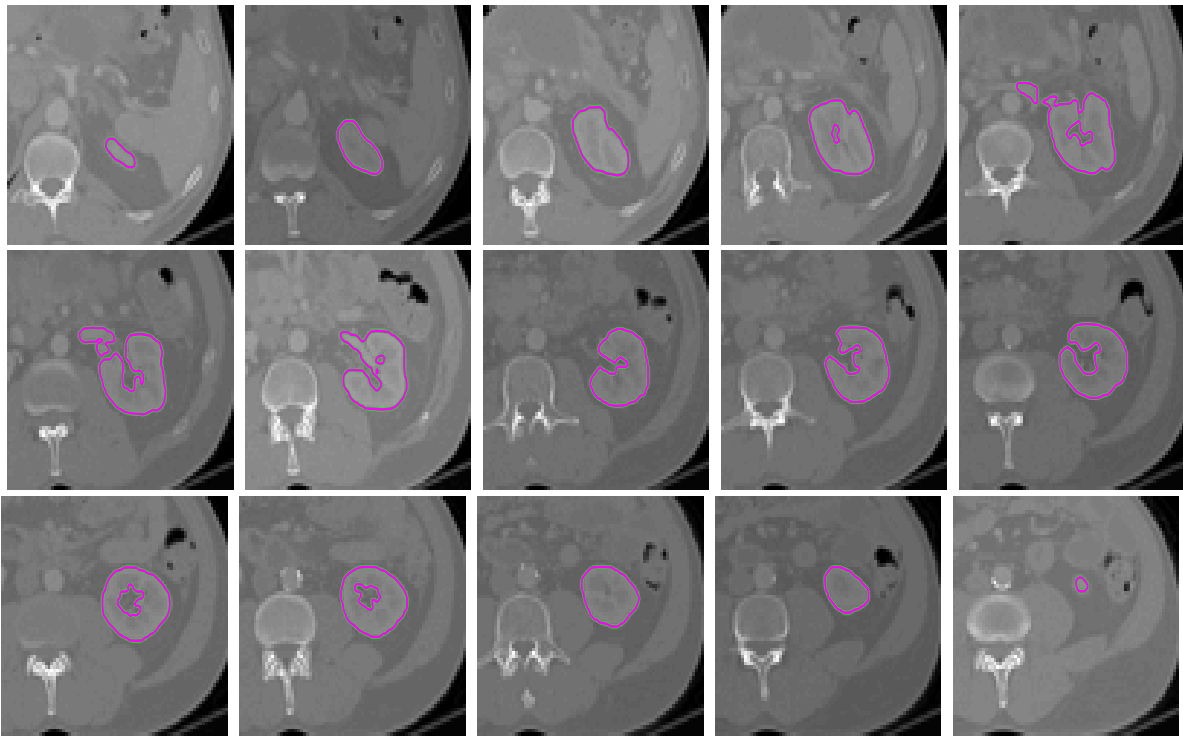
(c)



(d)



(e)



(f)

Figure 8: Test2 for the complex shape problem. (a) Original datum: slice-representation and marker sets in three slices(red dots are the markers); (b) and (d) Initial solution surface by our new strategy; (c) and (e) Successful result by our proposed method; (f) Slice-presentations of (e).

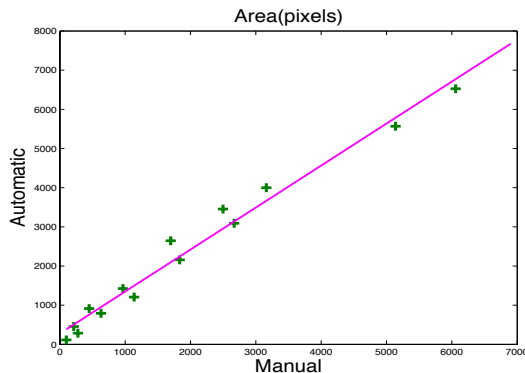


Figure 9: Comparison of our segmentation result with manual segmentation in detected areas.

in Figures 10(d)-10(f) and 10(j)-10(l). There, we also display the closeness to the manual detection by percentages in segmented areas for the concerned slices. Since the manually segmented organ volumes are not published, we compare all slices (numbered 40, 60, 68, 88, 100, 108, 120, 128, 140, 148, 160, 168, 180, 288) that have known manually segmented contours in Figure 9 segmented areas. In fact, our plot of area comparison is similar to the winning result described in [www.litislab.eu/rvsc/workshop/files/zuluaga.pdf/attachment\\_download/attachedFile](http://www.litislab.eu/rvsc/workshop/files/zuluaga.pdf/attachment_download/attachedFile) for volume comparison.

Secondly, the Patient 23 (from the test dataset) is used to test the performance of our algorithm in Figure 11(a)-11(h). Again, our method can be seen to yield satisfactory results.

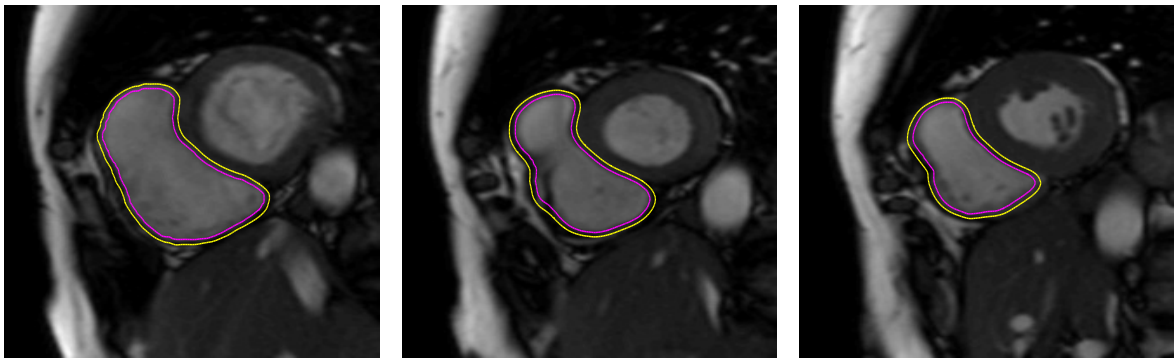
## 5 Conclusions

This paper presented an efficient segmentation model based on the geometrical constraints, an edge detector function and a markers distance function, capable of detecting a single object in 3D datum reliably. The efficiency is achieved by evolving the active surfaces in a narrow band sub-domain and re-initialization is done by a fast multigrid method. Test results show that the new algorithm performs better than the BC model [9] generalized to 3D and it is reliable for a range of challenging problems and robust in terms of segmentation quality. Future works will consider the local features based selective segmentation for texture images and other 3D segmentation frameworks.

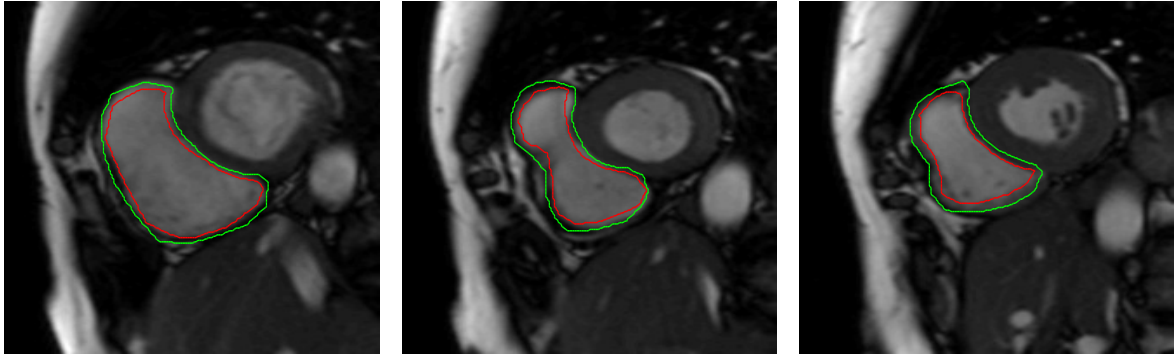
### Appendix 1 – Generation of an initial solution using $\mathcal{A}$

The initial solution  $\phi$  (i.e.  $\phi_0$ ) should take the value  $-1$  inside sub-domain containing the marker set  $\mathcal{A}$  and  $1$  outside it.

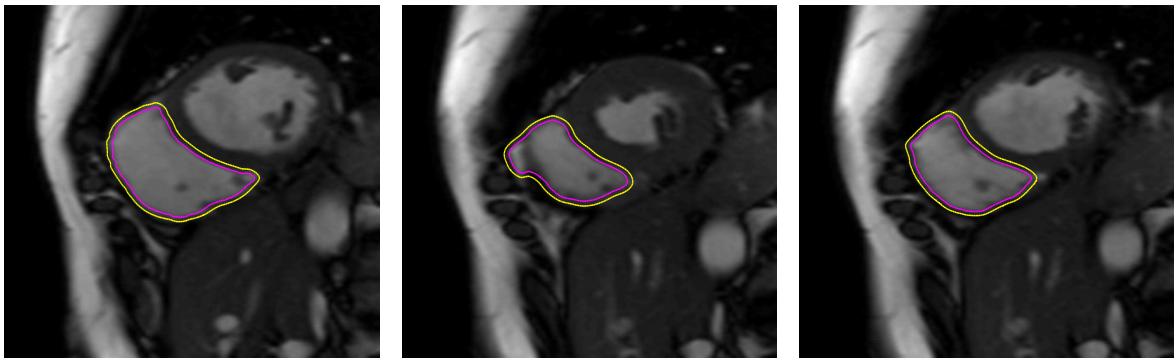
In previous work on 2D models, it can be a single curve (e.g. an ellipse or a square) if global segmentation is desired; for local and selective segmentation [9], one may use a polygon consisted of



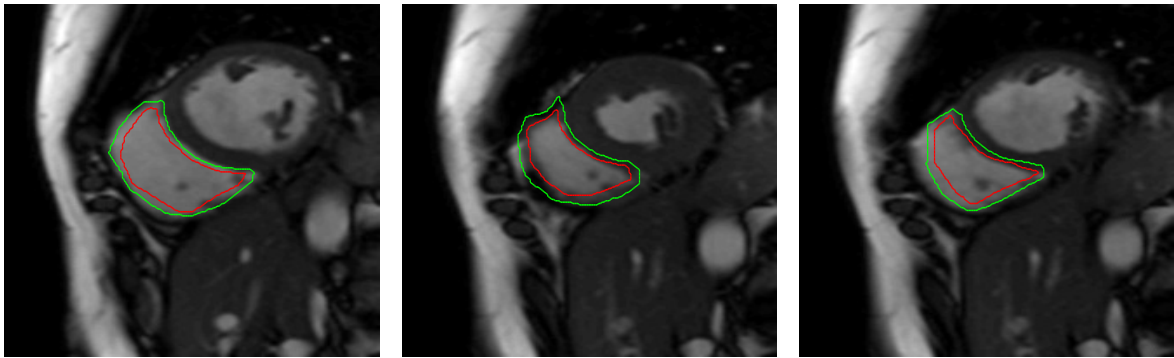
(a) automatic: 60th slice (98.79%) (b) automatic: 68th slice (98.13%) (c) automatic: 88th slice (97.15%)



(d) manual: 60th slice (e) manual: 68th slice (f) manual: 88th slice



(g) automatic: 100th slice (100%) (h) automatic: 108th slice (94.22%) (i) automatic: 120th slice (97.29%)



(j) manual: 100th slice (k) manual: 108th slice (l) manual: 120th slice

Figure 10: Comparative results by our algorithm for Patient 12 (the training set). Our 3D selective segmentation results for different slice representations: Figure 10(a)-10(i); manual results of the training set: Figure 10(d)-10(l). Here % values are for  $RSMr$ , comparing our automatic algorithm with the manual segmentation.

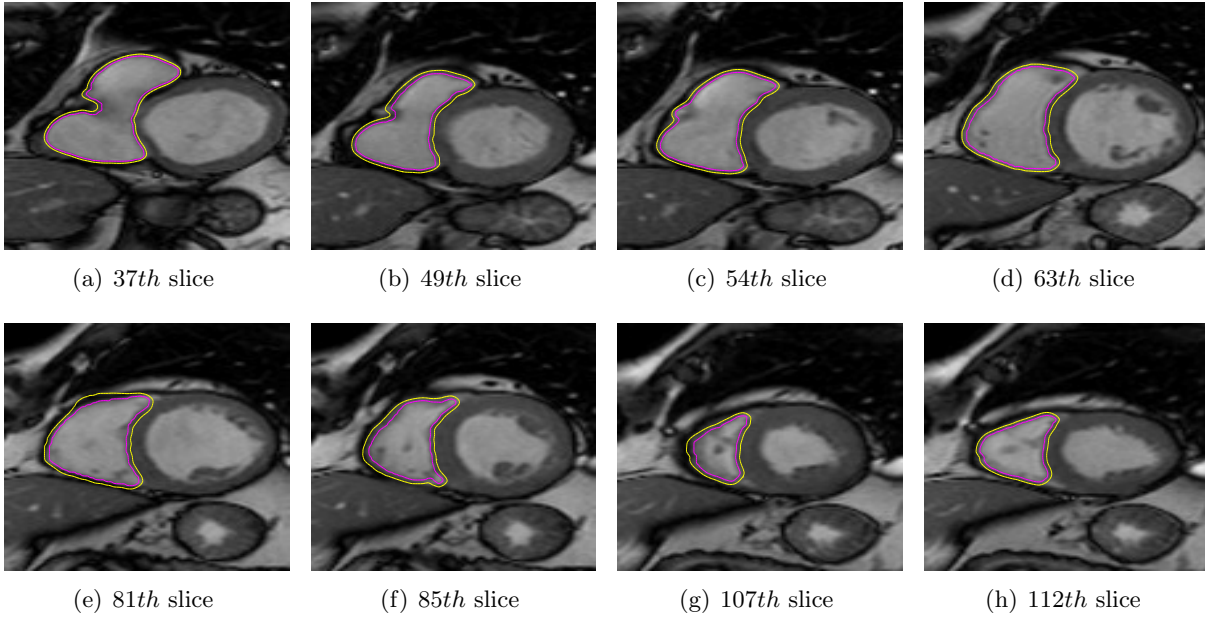


Figure 11: Comparative results by our automatic algorithm for Patient 23 (the test1 set).

points in the given marker set assuming that it contains three or more points. However in 3D, the initial guess can be nontrivial, to allow generality.

Here we assume that our 3D object is present in many slices (e.g. 400) and a user has given marker sets on 3 slices only. On at least two slices we need 3 or more markers in order to construct an initial surface  $\phi$  in 3D. Without losing generality, we consider how to link up the markers in the first two adjacent slices to form the initial  $\phi_0$ .

Suppose that on the first marker slice the marker set  $\mathcal{A}_1^{00} = \{p_i : 1 \leq i \leq m_1\}$  is given in anticlockwise order and on the second marker slice we have  $\mathcal{A}_2^{00} = \{p_i : m_1 + 1 \leq i \leq m_1 + m_2\}$  also in anticlockwise order. If  $m_1 = 6, m_2 = 4$  we have  $\mathcal{A}_1^{00} = \{01, 02, 03, 04, 05, 06\}$  and  $\mathcal{A}_2^{00} = \{07, 08, 09, 10\}$  (see Fig.12(a)). For later use, define by  $d(p, \mathcal{A}) = \min_{p_i \in \mathcal{A}} d(p, p_i)$  the distance between point  $p$  and the marker set  $\mathcal{A}$  and accordingly by  $I(p, \mathcal{A}) = \arg \min_i |d(p, p_i) - d(p, \mathcal{A})|$  the index number achieving the minimal distance. That is,  $d(p, \mathcal{A}) = d(p, p_{I(p, \mathcal{A})})$ .

Our algorithm below will first locate the nodes which define the ‘diameter’ of the implicit polygon on each slice; these nodes will be connected across slices and they divide each marker set into 2 overlapping subsets. Next we recursively subdivide the subsets until each corresponding subset pair makes up one unique triangle (i.e. one set having 1 node and the other having two) and then the corresponding nodes will be connected across slices. Unless both slices have the same number of nodes, typically, two or more nodes from one slice may be connected to the same node on the other slice.

Here is our proposed algorithm for computing the initial  $\phi_0$ :

- i). **Step 1 – First two edge pairs.** Compute the respective center points  $Pc1$  and  $Pc2$  of  $\mathcal{A}_1^{00}$ ,  $\mathcal{A}_2^{00}$ . Then through these center points we draw lines along x-direction and y-direction intersecting with the boundary  $\partial\Omega$  at  $a_i$ ,  $b_i$ ,  $c_i$ ,  $d_i$  (anticlockwise) respectively for  $i = 1$  (slice 1), 2 (slice 2); note on slice 1,  $a_1, c_1$  are along the x-direction.

To obtain a good approximation to the shape of the desired object, the first two edge pairs defining the ‘diameter’ of the polygon formed by the markers on each slice will be most important. Specifically, if

$$\sum_{i=1}^2 (d(a_i, \mathcal{A}_i^{00}) + d(c_i, \mathcal{A}_i^{00})) \leq \sum_{i=1}^2 (d(b_i, \mathcal{A}_i^{00}) + d(d_i, \mathcal{A}_i^{00}))$$

then the x-direction oriented pairs  $\{\hat{I}_1, \check{I}_1\} \equiv \{I(a_1, \mathcal{A}_1^{00}), I(a_2, \mathcal{A}_2^{00})\}$  and  $\{\hat{I}_2, \check{I}_2\} \equiv \{I(c_1, \mathcal{A}_1^{00}), I(c_2, \mathcal{A}_2^{00})\}$  are chosen as the first two edge-pairs; else if the above condition is not satisfied, the two y-direction oriented edge-pairs  $\{\hat{I}_1, \check{I}_1\} \equiv \{I(b_1, \mathcal{A}_1^{00}), I(b_2, \mathcal{A}_2^{00})\}$  and  $\{\hat{I}_2, \check{I}_2\} \equiv \{I(d_1, \mathcal{A}_1^{00}), I(d_2, \mathcal{A}_2^{00})\}$  are chosen. Further the marker sets  $\mathcal{A}_1^0$  and  $\mathcal{A}_2^0$  are split into four overlapping parts  $\mathcal{A}_1^{10}$ ,  $\mathcal{A}_1^{11}$ ,  $\mathcal{A}_2^{10}$ , and  $\mathcal{A}_2^{11}$  or two corresponding subset pairs  $\mathcal{A}_1^{10}—\mathcal{A}_2^{10}$ ,  $\mathcal{A}_1^{11}—\mathcal{A}_2^{11}$  along the chosen coordinate direction.

We illustrate the selection idea in Fig.12(b) where  $\{\hat{I}_1, \check{I}_1\} = \{02, 08\}$  and  $\{\hat{I}_2, \check{I}_2\} = \{06, 10\}$ . Subsequently  $\mathcal{A}_1^{10} = \{06, 01, 02\}$ ,  $\mathcal{A}_1^{11} = \{02, 03, 04, 05, 06\}$ ,  $\mathcal{A}_2^{10} = \{10, 07, 08\}$  and  $\mathcal{A}_2^{11} = \{08, 09, 10\}$ .

- ii). **Step 2 – Recursive splitting of corresponding subsets.** The obtained subsets of markers will be connected up next; the task is easy if all contain a single node and, if not, we recursively split them simultaneously across the 2 slices until one subset in all subset pairs contains a single node or only 2 nodes. Our idea of subdividing is to ensure the vertical distance of a subset dividing line is minimal. Note that the total number of nodes in a subset pair is at least 3.

For simplicity, consider the subset pair  $\mathcal{A}_1^{10}$  and  $\mathcal{A}_2^{10}$ . Three cases may occur. Firstly, when either  $\mathcal{A}_1^{10}$  or  $\mathcal{A}_2^{10}$  has a single node, then connect this single point to all points of another marker set and return the corresponding triangles. Secondly when either  $\mathcal{A}_1^{10}$  or  $\mathcal{A}_2^{10}$  has exactly 2 nodes; suppose  $\mathcal{A}_1^{10} = \{p_1^{10}, p_2^{10}\}$  and  $\mathcal{A}_2^{10} = \{q_j^{10} : 1 \leq j \leq m, m \geq 2\}$ . The split of  $\mathcal{A}_1^{10}$  is easy. Then the node in  $\mathcal{A}_2^{10}$  that can minimize both  $d(p_1^{10}, \mathcal{A}_2^{10} \setminus \{q_1^{10}\})$  and  $d(p_2^{10}, \mathcal{A}_2^{10} \setminus \{q_m^{10}\})$  is used to split the other subset. The new pairs of subsets fall into the first case. Thirdly, when index numbers of both marker sets are more than 2, especially take  $\mathcal{A}_1^{10} = \{p_i^{10} : 1 \leq i \leq n, n > 2\}$  and  $\mathcal{A}_2^{10} = \{q_j^{10} : 1 \leq j \leq m, m > 2\}$ , and find  $d(p_i^{10}, q_j^{10}) = d(\mathcal{A}_1^{10} \setminus \{p_1^{10}, p_n^{10}\}, \mathcal{A}_2^{10} \setminus \{q_1^{10}, q_m^{10}\})$ ; then the corresponding edge-pair  $p_i^{10}—q_j^{10}$  splits the marker sets  $\mathcal{A}_1^{10}$  and  $\mathcal{A}_2^{10}$  into four parts or two corresponding subset pairs. Further recursively repeat the above process until all subset pairs go through the first case; see Fig.12(c)-12(e) for one example. Finally triangulating in each of

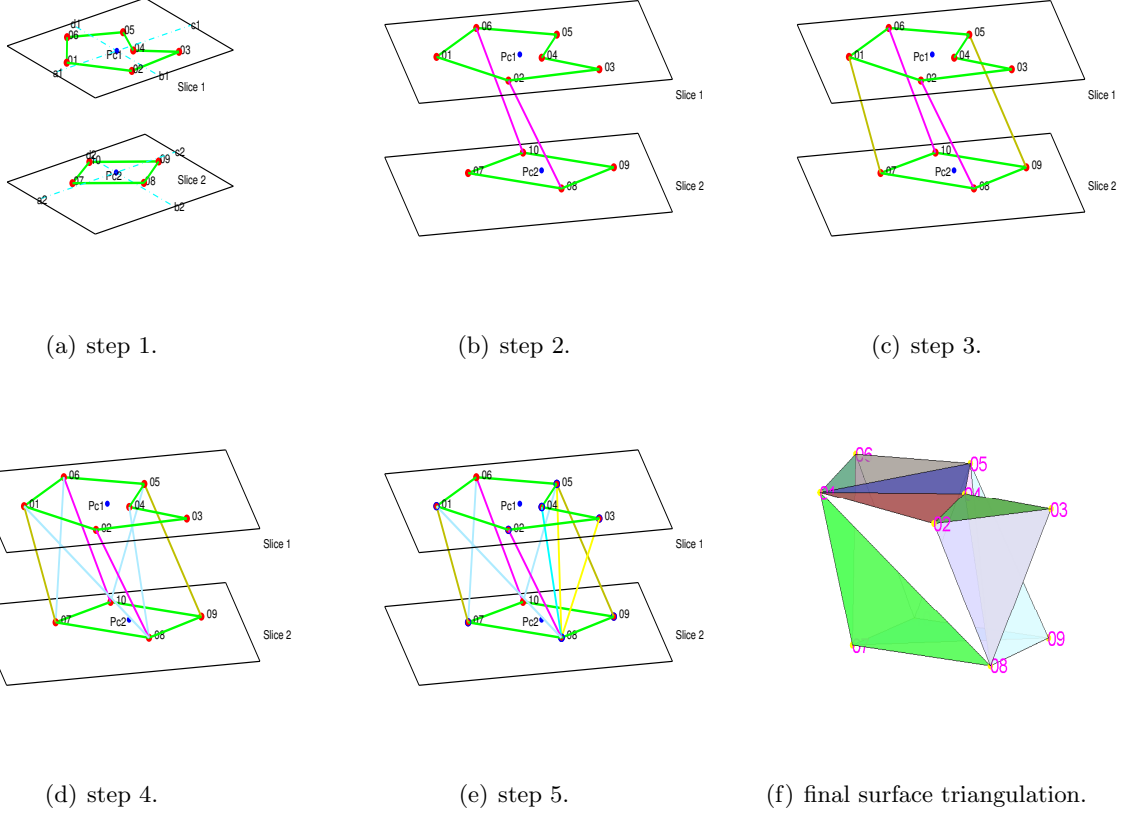


Figure 12: Generation of polyhedral surface by our strategy.

slice 1 and slice 2 to obtain all triangles, we arrive at a polyhedral surface (as in Fig.12(f)).

- iii). **Step 3 – Completion of the polyhedral surface.** Repeat Steps 1-2 for slice 2 and slice 3 to obtain the overall initial surface for  $\phi = 0$ . Compute outer normals of all triangles on the polyhedral surface to seek the inner region and outer region of the polyhedral surface by the algorithm from [53] and complete the initial level set function  $\phi_0$  such that  $\Gamma = \{x \in \Omega : \phi_0(x) = 0\}$ ,  $\Omega_{in} = \{x \in \Omega : \phi_0(x) < 0\}$  and  $\Omega_{out} = \{x \in \Omega : \phi_0(x) > 0\}$ .

Figure 13 shows two initial solution strategies for a group of user-supplied marker sets in three dimensions. On the left three slices of 3D datum are shown on 3D cubic space that contains marker sets (red dots). On the middle the initial zero level surface constructed by the simplex surface strategy is represented in a neighborhood of three slices. We show the initial zero level surface constructed by our strategy on the right.

## Acknowledgments

The work is partially supported by Royal Liverpool University Hospital UK, the UK EPSRC EP/K036939/1 and the National Natural Science Foundation of China (11301447).

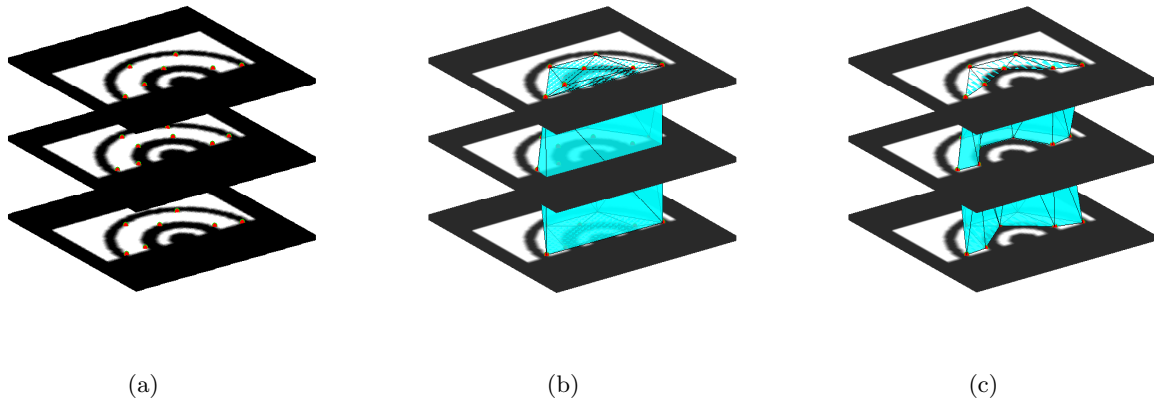


Figure 13: Initial solution selection strategies. (a) Original datum slices and marker sets in three slices (red dots are the markers); (b) Initial solution surface by simplex strategy; (c) Initial solution surface by our new strategy.

## References

- [1] D. Adalsteinsson and J. A. Sethian. A fast level set method for propagating interfaces. *J. Comput. Phys.*, 118(2):269–277, 1995.
- [2] D. Adalsteinsson and J. A. Sethian. A level set approach to a unified model for etching, deposition, and lithography. II. 3D simulations. *J. Comput. Phys.*, 122(2):348–366, 1995.
- [3] J. C. Adams. Mudpack-2: multigrid software for approximating elliptic partial differential equations on uniform grids with any resolution. *Appl. Math. Comput.*, 53:235–249, 1993.
- [4] L. Ambrosio and V. Tortorelli. Approximation of functionals depending on jumps by elliptic functionals via  $\Gamma$ -convergence. *Comm. Pure Appl. Math.*, 43:999–1036, 1990.
- [5] B. Appleton and H. Talbot. Globally optimal geodesic active contours. *J. Math. Imaging Vis.*, 23(1):67–86, 2005.
- [6] G. Aubert and P. Kornprobst. *Mathematical Problems In Image Processing: Partial Differential Equations and the Calculus Of Variations*. Springer-Verlag, New York, 2002.
- [7] N. Badshah and K. Chen. Multigrid method for the Chan-Vese model in variational segmentation. *Commun. Comput. Phys.*, 4(2):294–316, 2008.
- [8] N. Badshah and K. Chen. On two multigrid algorithms for modeling variation multiphase image segmentation. *IEEE Trans. Image Process*, 18(5):1097–1106, 2009.
- [9] N. Badshah and K. Chen. Image selective segmentation under geometrical constraints using an active contour approach. *Commun. Comput. Phys.*, 7(4):759–778, 2010.

- [10] T. Brox and D. Cremers. On the statistical interpretation of the piecewise smooth Mumford-Shah functional. In *Proceedings of the 1st int. conf. on Scale space and variational methods in computer vision*, SSVM'07, pages 203–213, Berlin, Heidelberg, 2007. Springer-Verlag.
- [11] X. Cai, R. H. Chan, and T. Y. Zeng. A two-stage image segmentation method using a convex variant of the mumford-shah model and thresholding. *SIAM J. Imaging Sci.*, 6:368–390, 2013.
- [12] V. Caselles, Francine Catté, Tomeu Coll, and Françoise Dibos. A geometric model for active contours in image processing. *Numer. Math.*, 66(1):1–31, 1993.
- [13] V. Caselles, R. Kimmel, and G. Sapiro. Geodesic active contours. *Int. J. Comput. Vis.*, 22(1):61–79, 1997.
- [14] V. Caselles, R. Kimmel, Guillermo Sapiro, and Catalina Sbert. Minimal surfaces based object segmentation. *IEEE Trans. PAMI*, 19(4):394–398, April 1997.
- [15] T. F. Chan, S. Esedoglu, and M. Nikilova. Algorithms for finding global minimizers of image segmentation and denoising models. *SIAM J. Appl. Math.*, 66:1932–1648, 2006.
- [16] T. F. Chan and J. H. Shen. *Image Processing and Analysis: Variational PDE, Wavelet, and Stochastic Methods*. SIAM publications, Philadelphia, PA, 2005.
- [17] T. F. Chan and L. A. Vese. An efficient variational multiphase motion for the Mumford-Shah segmentation model. In *2000 Conference Record of the 34<sup>th</sup> Asilomar Conf. on Signals, Systems and Computers*, volume 1, pages 490–494, 2000.
- [18] T. F. Chan and L. A. Vese. Active contours without edges. *IEEE Trans. Image Process.*, 10(2):266–277, 2001.
- [19] T. F. Chan and L. A. Vese. Active contour and segmentation models using geometric PDE's for medical imaging. In *Geometric methods in bio-medical image processing*, Math. Vis., pages 63–75. Springer, Berlin, 2002.
- [20] D. L. Chopp. Computing minimal surfaces via level set curvature flow. *J. Comput. Phys.*, 106(1):77–91, 1993.
- [21] I. Cohen, L. D. Cohen, and N. Ayache. Using deformable surfaces to segment 3D images and infer differential structures. In *Proceedings of the 2nd European conf. on computer vision*, ECCV '92, pages 648–652, London, UK, 1992. Springer-Verlag.
- [22] L. D. Cohen. On active contour models and balloons. *CVGIP: Image Underst.*, 53(2):211–218, March 1991.

- [23] S. Corsaro, K. Mikula, A. Sarti, and F. Sgallari. Semi-implicit covolume method in 3D image segmentation. *SIAM J. Sci. Comput.*, 28(6):2248–2265, 2006.
- [24] C. Darolti, A. Mertins, C. Bodensteiner, and U. G. Hofmann. Local region descriptors for active contours evolution. *IEEE Trans. Image Process.*, 17(12):2275–2288, 2008.
- [25] R. Goldenberg, R. Kimmel, E. Rivlin, and M. Rudzsky. Fast geodesic active contours. *IEEE Trans. Image Process.*, 10(10):1467–1475, 2001.
- [26] R. Goldenberg, R. Kimmel, E. Rivlin, and M. Rudzsky. Cortex segmentation: a fast variational geometric approach. *IEEE Trans. Med. Imaging*, 21(12):1544–1551, 2002.
- [27] C. Gout, C. Le Guyader, and L. A. Vese. Segmentation under geometrical conditions using geodesic active contours and interpolation using level set methods. *Numer. Algorithms*, 39(1-3):155–173, 2005.
- [28] Y. Gu, L. L. Wang, and X. C. Tai. A direct approach towards global minimization for multiphase labeling and segmentation problems. *IEEE Trans. Image Proc.*, 21:2399 – 2411, 2012.
- [29] M. Holtzman-Gazit, R. Kimmel, N. Peled, and D. Goldsher. Segmentation of thin structures in volumetric medical images. *IEEE Trans. Image Process.*, 15(2):354–363, 2006.
- [30] M. Jeon, M. Alexander, W. Pedrycz, and N. Pizzi. Unsupervised hierarchical image segmentation with level set and additive operator splitting. *Pattern Recognition Letters*, 10-26:1461–1469, 2005.
- [31] M. Y. Jung, X. Bresson, T. F. Chan, and L. A. Vese. Nonlocal Mumford-Shah regularizers for color image restoration. *IEEE Trans. Image Process.*, 20(6):1583–1598, June 2011.
- [32] M. Kass, A. Witkin, and D. Terzopoulos. Snakes: Active contour models. *Int. J. Comput. Vis.*, 1(4):321–331, 1988.
- [33] S. Lankton and A. Tannenbaum. Localizing region-based active contours. *IEEE Trans. Image Process.*, 17(11):2029–2039, 2008.
- [34] C. Li, C. Xu, C. Gui, and M. D. Fox. Level set evolution without re-initialization: A new variational formulation. *IEEE Computer Society Conference on Computer Vision and Pattern Recognition*, 1:430–436, 2005.
- [35] C. Li, C. Xu, C. Gui, and M. D. Fox. Distance regularized level set evolution and its application to image segmentation. *IEEE Trans. Image Process.*, 19:3243–3254, 2010.
- [36] C. M. Li, C. Y. Kao, J. C. Gore, and Z. H. Ding. Minimization of region-scalable fitting energy for image segmentation. *IEEE Trans. Image Process.*, 17(10):1940–1949, 2008.

- [37] F. Li, M. K. Ng, and C. M. Li. Variational fuzzy Mumford-Shah model for image segmentation. *SIAM J. Appl. Math.*, 70(7):2750–2770, 2010.
- [38] J. Liu, X.-C. Tai, H. Y. Huang, and Z. D. Huan. A fast segmentation method based on constraint optimization and its applications: intensity inhomogeneity and texture segmentation. *Pattern Recogn.*, 44(9):2093–2108, 2011.
- [39] R. Malladi, R. Kimmel, D. Adalsteinsson, G. Sapiro, V. Caselles, and J. A. Sethian. A geometric approach to segmentation and analysis of 3d medical images. In *Proceedings of the 1996 Workshop on Mathematical Methods in Biomedical Image Analysis*, MMBIA '96, pages 244–252, Washington DC, USA, 1996. IEEE Computer Society.
- [40] R. Malladi, J. A. Sethian, and Baba C. Vemuri. Shape modeling with front propagation: A level set approach. *IEEE Trans. PAMI*, 17(2):158–175, 1995.
- [41] J. Mille. Narrow band region-based active contours and surfaces for 2D and 3D segmentation. *Comput. Vis. Image Underst.*, 113(9):946–965, 2009.
- [42] B. Mory and R. Ardon. Fuzzy region competition: A convex two-phase segmentation framework. *Proc of Scale Space and Variational Methods in Computer Vision*, 4485:214–226, 2007.
- [43] D. Mumford and J. Shah. Optimal approximations by piecewise smooth functions and associated variational problems. *Comm. Pure Appl. Math.*, 42(5):577–685, 1989.
- [44] S. Osher and R. Fedkiw. *Level set methods and dynamic implicit surfaces*. Springer-Verlag, New York, 2003.
- [45] L. Rada and K. Chen. A new variational model with dual level set functions for selective segmentation. *Commun. Comput. Physics*, 12(1):261–283, 2012.
- [46] J. H. Shen.  $\Gamma$ -Convergence Approximation to Piecewise Constant Mumford-Shah Segmentation, volume 3708, chapter Advanced Concepts for Intelligent Vision Systems, pages 499–506. 2005.
- [47] K. W. Sum and P. Y. S. Cheung. A novel active contour model using local and global statistics for vessel extraction. In *28th Annual International Conference of the IEEE on Engineering in Medicine and Biology Society*, pages 3126–3129, 2006.
- [48] X.-C. Tai, O. Christiansen, P. Lin, and I. Skjælaaen. Image segmentation using some piecewise constant level set methods with mbo type of projection. *Int. J. Comput. Vis.*, 73:61–76, 2007.
- [49] D. Terzopoulos and D. Metaxas. Dynamic 3D models with local and global deformations: Deformable superquadrics. *IEEE Trans. PAMI*, 13(7):703–714, July 1991.

- [50] D. Terzopoulos, Andrew P. Witkin, and M. Kass. Constraints on deformable models: Recovering 3D shape and nonrigid motion. *Artif. Intell.*, 36(1):91–123, 1988.
- [51] A. Tsai, A. R. Yezzi, and A. S. Willsky. Curve evolution implementation of the Mumford-Shah functional for image segmentation, denoising, interpolation, and magnification. *IEEE Trans. Image Process.*, 10(8):1169–1186, 2001.
- [52] L. A. Vese and T. F. Chan. A multiphase level set framework for image segmentation using the Mumford-Shah model. *Int. J. Comp. Vis.*, 50(3):271–293, 2002.
- [53] W.-C. Wang and E. H. Wu. A new method for deciding whether a point is in a polygon or a polyhedron. *Journal of Software*, 11(12):1614–1619, 2000.
- [54] A. J. Yezzi Jr. *Curvature-driven flows for 2D and 3D image segmentation, smoothing, and enhancement*. 1997. PhD Thesis – University of Minnesota, USA.
- [55] Y. Zheng and K. Chen. A general model for multiphase texture segmentation and its applications to retinal image analysis. *Biomed. Signal Process. Control*, 8:374–381, 2013.
- [56] S. C. Zhu and A. Yuille. Region competition: unifying snakes, region growing, and Bayes/MDL for multiband image segmentation. *IEEE Trans. PAMI*, 18(9):884–900, 1996.